Cell Reports

Article

Spatiotemporal coordination of Slit-Robo repulsion and neurturin-Gfrα attraction guides multipolar migration during retinal lamination

Graphical abstract

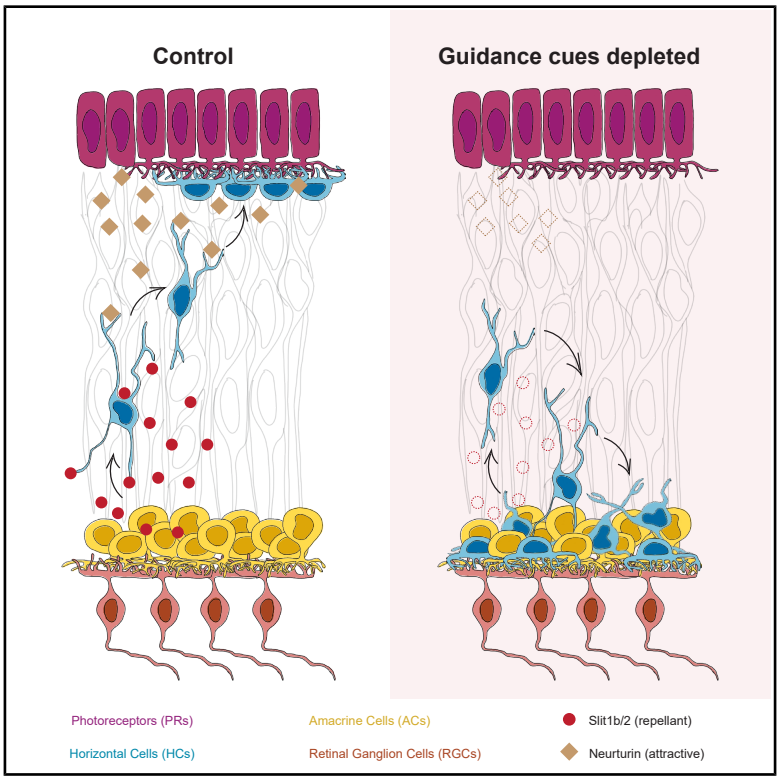

Highlights

- RNA-seq-guided CRISPR screen reveals guidance cues involved in horizontal cell positioning
- Repulsive Slit1b/2-Robo2 signaling steers horizontal cells out of the amacrine cells
- Neurturin-Gfrα1/2-Ret attraction ensures horizontal cell positioning beneath photoreceptors
- Interference with these cues impairs neuronal patterning in the vertebrate retina

Authors

Jaakko I. Lehtimäki, Jingtao Lilue, Margarida R. Cruz, Mario Del Rosario, Elisa Nerli, Ricardo Henriques, Caren Norden

Correspondence

jaakko.lehtimaki@abo.fi (J.I.L.), caren.norden@gimm.pt (C.N.)

In brief

Lehtimäki et al. reveal how repulsive Slit1b/2-Robo2 and attractive neurturin-Gfrα1/2-Ret signaling jointly coordinate multipolar migration of horizontal cells through crowded, scaffold-free environments of the vertebrate retina. This work was enabled by sophisticated transcriptomics analysis, targeted F0 CRISPR screening, and 3D fixed and live imaging.

Lehtimäki et al., 2026, Cell Reports *45*, 116948
February 24, 2026
https://doi.org/10.1016/j.celrep.2026.116948

CellPress

Cell Reports

CellPress
OPEN ACCESS

Article

Spatiotemporal coordination of Slit-Robo repulsion and neurturin-Gfrα attraction guides multipolar migration during retinal lamination

Jaakko I. Lehtimäki,[1,2,3,*] Jingtao Lilue,[1,4] Margarida R. Cruz,[1,2] Mario Del Rosario,[1,5] Elisa Nerli,[1,6,7] Ricardo Henriques,[1,5,8] and Caren Norden[1,2,9,*]

[1]Instituto Gulbenkian de Ciência (IGC), 2780-156 Oeiras, Portugal
[2]Gulbenkian Institute for Molecular Medicine (GIMM), 2780-156 Oeiras, Portugal
[3]InFLAMES Research Flagship Center, University of Turku and Åbo Akademi University, 20520 Turku, Finland
[4]Oujiang Laboratory (Zhejiang Lab for Regenerative Medicine, Vision, and Brain Health), Wenzhou 325000, China
[5]Instituto de Tecnologia Química e Biológica António Xavier, Universidade Nova de Lisboa, 2780-157 Oeiras, Portugal
[6]Max Planck Institute of Molecular Cell Biology and Genetics, 01307 Dresden, Germany
[7]Cluster of Excellence Physics of Life, Technische Universität Dresden, 01307 Dresden, Germany
[8]UCL Laboratory for Molecular Cell Biology, University College London, London WC1E 6BT, UK
[9]Lead contact
*Correspondence: jaakko.lehtimaki@abo.fi (J.I.L.), caren.norden@gimm.pt (C.N.)
https://doi.org/10.1016/j.celrep.2026.116948

SUMMARY

Multipolar migration is a conserved neuronal migration mode in the developing brain, enabling emerging neurons to navigate in crowded environments and reach precise laminar positions. Yet, how these cells interpret external cues to guide their migration is not fully understood. We investigate this question using retinal horizontal cells as a model. Combining transcriptomics, targeted CRISPR screening, and live imaging, we reveal the spatiotemporal guidance system underlying horizontal cell lamination: repulsive Slit1b/2-Robo2 signaling in the amacrine cell layer initiates apical horizontal cell migration, while attractive neurturin-Gfrα1/2 signaling from photoreceptors fine-tunes final positioning beneath the photoreceptor layer. Disruption of these pathways causes basal retention of horizontal cells, highlighting the importance of spatially coordinated signaling for proper lamination and functional retinal circuitry. Our results uncover how positional signals and tissue architecture cooperate to achieve neuronal migration precision, a principle likely relevant across the developing central nervous system.

INTRODUCTION

Most emerging neurons are born away from their final functional location and travel long distances before establishing functional neuronal circuits. During this journey, neurons must interpret spatial, chemical and mechanical cues.[1–3] When these cues are misread or disrupted, neurons can end up at ectopic locations which often leads to severe brain developmental defects.[4–6] Radially and tangentially migrating neurons, such as cortical excitatory neurons and inhibitory interneurons, have been extensively studied, particularly in the rodent neocortex. These studies revealed intracellular, intercellular, ECM-related, and classical axon-guidance mechanisms that drive the stereotypic migration and polarization of these cells, ultimately producing neuronal layering and lamination.[2,7–9]

However, cortical neurons can also move via multipolar migration, characterized by frequent directional changes, multiple dynamic protrusions, and the lack of stable attachments.[10–12] Neurons undergoing multipolar migration are prevalent across brain regions, including the neocortex, hippocampus, and retina. Further, this migration mode is conserved across vertebrates, occurring in fish, reptiles, chick, rodents, and ferrets.[10–17] In reptiles and chick, multipolar migration is the dominant migration mode responsible for cortical layering.[18] Despite this prevalence, the mechanisms guiding multipolar migration are less explored than those of radial and tangential modes, and how these cells navigate through the crowded brain tissue remains poorly understood.

To uncover the principles guiding multipolar migration, we investigate the migration of retinal interneurons, horizontal cells (HC), in the transparent zebrafish retina. The retina, part of the CNS reacting to visual stimuli, shows a highly conserved laminar architecture across vertebrates.[19,20] Out of five neuronal cell types in the developing retina, photoreceptors (PR), bipolar cells (BC), retinal ganglion cells (RGC), amacrine cells (AC), and HCs, multipolar migration has been observed for all except BCs. HCs most prominently exhibit this migration mode, traveling bidirectionally across the developing inner nuclear layer (INL)[21–29] (Figures 1A, 1B, and S1A and Video S1). Following this phase, mature HCs settle beneath the PR cell

layer to modulate visual signals within the conserved retinal circuit.[30]

Prior work showed that HC multipolar migration takes place in an environment without prominent ECM or notable stiffness gradients.[31] While the dynamics of migrating multipolar HCs[24,31] have been documented, how these cells interpret their environment to find their precise laminar positioning remains unclear. In particular, the factors triggering timely HC departure from the basal AC layer and guiding their non-stereotypic migration toward the PR layer are not well understood.

Here, we reveal guidance molecules that steer reproducible HC multipolar migration. By systemically probing the influence of neighboring retinal cell types on HC navigation and combining cell-type-specific transcriptomics using an *in vivo* CRISPR screen, we identify the ligand-receptor interactions between HCs and their changing environment. We find that HCs interpret spatially distinct attractive and repulsive cues, potentially through their dynamic protrusions, to integrate directional information as they move. These findings define a molecular framework for multipolar migration in complex environments lacking classical ECM-based or cellular scaffolds, which may represent a generalizable strategy for multipolar migration in the developing brain and beyond.

RESULTS

Multipolar horizontal cell migration occurs independently of bipolar cells

When leaving the AC layer, multipolar HCs take individual paths to reach their final laminar position below the PRs.[24] The part of the INL through which HCs move is mainly occupied by BCs at a developmental stage when BC nuclei approach theoretical packing limits[32,33] (Figure 1C). We thus asked whether BCs could influence ECM-independent multipolar HC migration. We depleted BCs by targeting both Vsx1 and Vsx2 transcription factors, crucial for determining BC fate.[34,35] We injected Cas9/gRNA ribonucleoprotein complexes (RNPs) targeting three loci in both *vsx1* and *vsx2*, to generate F0 knockout (KO) embryos[36] in a *Tg(vsx1:GFP); Tg(ptf1a:DsRed)* reporter line. This line labels both, possibly remaining BCs (via vsx1) and retinal interneurons (HCs and ACs, via ptf1a). Consistent with previous reports showing general robustness of retinal architecture upon depletion of different neuronal populations,[37–39] *vsx1+vsx2* KO embryos showed INL lamination similar to controls with the volume normally occupied by BCs being filled by DsRed-positive cells, most likely ACs (Figure S1B). Performing the same knockout in a *Tg(lhx1:GFP); Tg(ptf1a:DsRed)* reporter line labeling both HCs (lhx1 and ptf1a) and ACs (ptf1a), we found that HC migration and lamination were largely unaffected by the absence of BCs (Figures 1D and 1F). Further, *in vivo* imaging of the developing *vsx1+vsx2* F0 KO retina revealed no obvious differences in HC apical migration dynamics (Video S1). Together, this suggests that whereas BCs are crucial for visual stimuli processing in mature retinae,[34] they do not provide guidance, nor function as a physical scaffold to migrating multipolar HCs.

Photoreceptor cell depletion causes horizontal cells to overshoot to ectopic apical positions

In the absence of BCs, migrating HCs still reach their final position beneath the PRs, with which they later form synaptic networks to process visual stimuli.[40] This raised the possibility that PRs attract multipolar migrating HCs. To test this idea, we interfered with PR-fate specification. We chose CRISPR-mediated depletion of Prdm1a and Prdm1b transcription factors, as Prdm1a morpholinos cause general retinal lamination defects and a developmental delay.[38,41] We analyzed the phenotypes directly in the F0 generation[36] using a pan-reporter for early neurogenic progenitors and different types of early neurons *Tg(atoh7:gap-RFP)* and a reporter for both HCs and early PRs *Tg(lhx1:GFP)*.[26,38]

Whereas retinal lamination in *prdm1a* KOs seemed similar to controls (Figures 1E and S1C), *prdm1b* KOs displayed patches without PRs in the most apical cell layer (Figures 1E and S1D). As combined *prdm1a* and *prdm1b* KOs showed no additive effects (Figure S1E), we focused on the *prdm1b* KOs.

The apical areas devoid of PRs were frequently occupied by ectopically placed HCs. Live-imaging of the KO embryos in *Tg(atoh7:gap-RFP*, labels PRs) and *Tg(lhx1:GFP*, labels HCs) reporter lines confirmed that migrating HCs can overshoot apically to positions where the PR layer was compromised (Video S1). We further noted a small but reproducible number of HCs that did not migrate apically but remained within the AC layer in *prdm1b* KO embryos. Such "stuck HCs" were not seen in control or in *scrambled* KOs (embryos injected with RNPs carrying non-targeting gRNAs[36]) (Figures 1F and S1D). This indicated that PRs have some guiding effect on HC migration, although this effect appeared minor. In places in which the PR layer was not formed, HCs overshot their normal position and resided there.

Together, these experiments suggest that, similar to basal RGCs (Figure 1A) that were reported to provide a physical stopping point for the HC initial basal movement,[31] PRs serve as a physical barrier for HC apical migration.

Horizontal cells fail to undergo multipolar apical migration in the absence of amacrine cells

We showed that BCs or PRs do not massively influence apical HC migration. Further, previous work revealed that also RGCs, while acting as a basal barrier in controls, are dispensable for overall HC migration.[31] We therefore examined whether ACs, which surround and intermingle with HCs at this developmental stage, could instruct HC movement. ACs and HCs both initially use somal translocation to migrate basally and then switch to a multipolar morphology within the AC layer.[15,42] Once in the AC layer, multipolar ACs laminate, showing only minor further movements, while HCs remain there for up to 8 h before initiating multipolar apical migration (Figures 1A and 1B). To test whether the neighboring ACs contribute to HC departure from the AC layer, we used two Ptf1a morpholinos (MOs), which together remove most ACs and substantially reduce the amount of HCs.[43,44] Morpholinos were injected into the reporter line *Tg(lhx1:GFP); Tg(ptf1a:DsRed)* labeling HCs and early PRs (via lhx1) and HCs and ACs (via ptf1a). In agreement with previous findings,[38,39] the MO-treated retinae at 72 hpf lacked almost all ACs and most HCs (Figure 2A). Remaining HCs in the MO-treated

CellPress
OPEN ACCESS

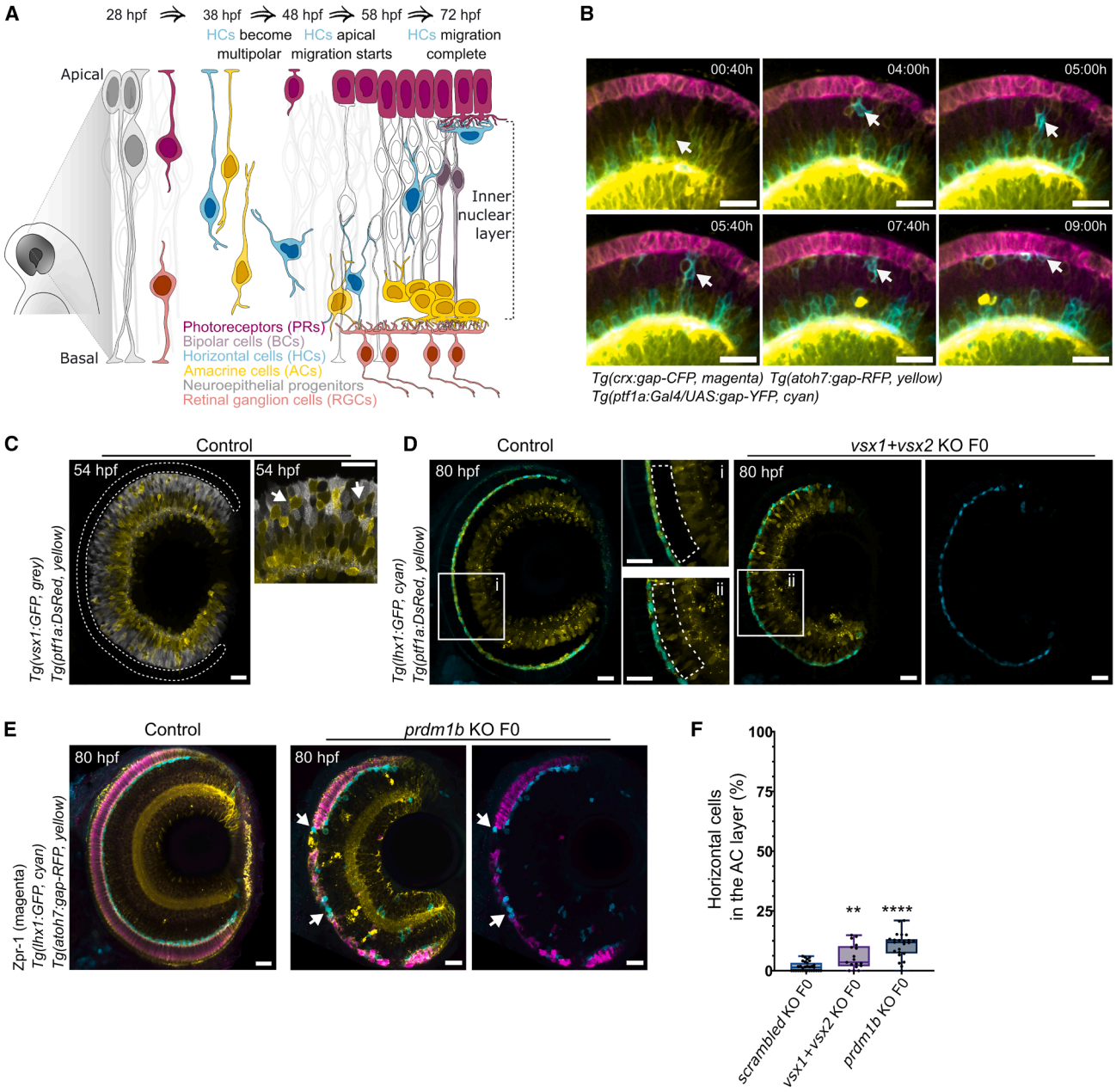

Figure 1. Multipolar horizontal cell navigation is not affected by bipolar cell absence or partial photoreceptor loss

(A) Schematic of multipolar horizontal cell (HC, cyan) migration in the developing zebrafish retina, relative to RGCs (red), ACs (yellow), PRs (magenta), and BCs (purple). See Figure S1A.

(B) Time series of HC (cyan/yellow; white arrow) multipolar migration from the basal AC layer (cyan and yellow) toward the PRs, culminating in lamination below the PR layer (magenta). RGC layer (yellow) resides below the ACs. *Tg(atoh7:gap-RFP)* labels all retinal neurons except BCs; *Tg(ptf1a:Gal4; UAS:gap-YFP)* labels ACs and HCs, and *Tg(crx:gap-CFP)* labels PRs and faintly BCs. Scale bars: 20 μm. See Video S1.

(C) Lamination of BCs (gray), Acs, and HCs (yellow) at 54 hpf. Dotted line area marks the PR layer. Right: magnified view showing migrating HCs (white arrows) between BCs. *Tg(vsx1:GFP)* marks BCs, and *Tg(ptf1a:DsRed)* marks ACs and HCs. Scale bars: 20 and 5 μm, respectively.

(D) HC and AC lamination at 80 hpf in control and *vsx1+vsx2* F0 KO embryos lacking BCs. In contrast to the control (i), in the KO retina (ii), the AC layer (yellow) extends into the presumptive BC layer (dashed line). *Tg(lhx1:GFP)* labels HCs, and *Tg(ptf1a:DsRed)* labels ACs and HCs. Scale bars: 20 μm. See Figure S1B and Video S1.

(E) HC (cyan, white arrows) migration in control and *prdm1b* F0 KO embryo showing gaps in the PR layer (magenta and yellow). Zpr-1 labels PRs, *Tg(lhx1:GFP)* labels HCs, *Tg(atoh7:gap-RFP)* labels PRs, HCs, and RGCs. Scale bars: 20 μm. See Video S1 and Figures S1D and S1E.

(F) Quantification of HCs >5 μm away from the PR layer in laminated retinae of different genetic conditions. $N = 31$ (control, *scrambled* KO), 17 (*vsx1+vsx2*), and 23 (*prdm1b*). p values (Mann-Whitney test vs. *scrambled* KO) = 0.0029 (*vsx1+vsx2* **); <0.0001 (*prdm1bl* ****). Boxes show interquartile range; center line = median; whiskers = min/max; dots = individual retinae.

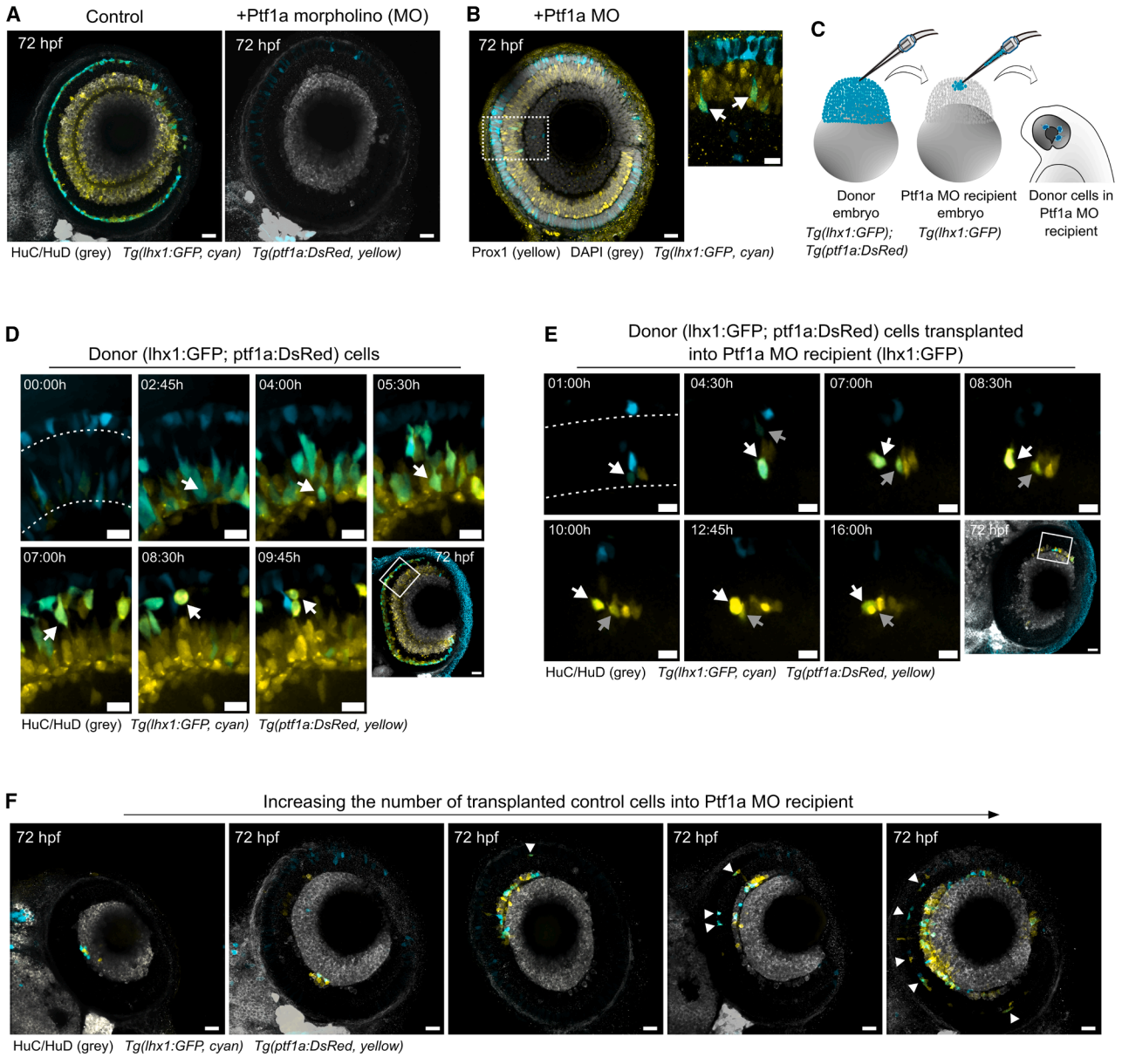

Figure 2. Horizontal cells fail to migrate apically in the absence of amacrine cells

(A) HCs (cyan/yellow) and ACs (gray/yellow) in control and Ptf1a morpholino (MO) embryos. *Tg(lhx1:GFP)* labels HCs and PRs, and *Tg(ptf1a:DsRed)* labels ACs and HCs. HuC/HuD (gray) labels ACs and RGCs. Scale bars: 20 μm.

(B) Ptf1a MO-treated retina stained for Prox1 (yellow), which labels BCs and HCs (white arrows). *Tg(lhx1:GFP)* labels HCs and PRs. Right: magnified region (dashed box). DAPI (gray) marks nuclei. Scale bars: 20 and 10 μm, respectively.

(C) Transplantation schematics. Control cells (cyan) from *Tg(lhx1:GFP); Tg(ptf1a:DsRed)* donors were transplanted into Ptf1a MO-treated recipient *Tg(lhx1:GFP)* (gray) at the midblastula stage.

(D) Time series of control HC migration (cyan and yellow, white arrow) in a donor retina. Dotted lines mark PR and AC layers. The last panel shows the same retina at 72 hpf (white box = imaged area). HuC/HuD (gray) labels ACs and RGCs. Scale bars: 5 and 20 μm, respectively. See Video S2.

(E) Time series of transplanted control HCs in a Ptf1a MO recipient retina. Control HCs (white and gray arrows) fail to migrate apically. The dotted lines indicate PR and AC layers. The last panel shows the same retina at 72 hpf (white box = imaged area). HuC/HuD (gray) labels ACs and RGCs. Scale bars: 10 and 20 μm, respectively. See Video S2.

(F) 72 hpf *Tg(lhx1:GFP)* Ptf1a MO-injected recipient retinae with increasing numbers of transplanted control ACs (yellow) and HCs (cyan and yellow). Arrowheads mark HCs successfully laminated beneath PRs. *Tg(lhx1:GFP)* labels HCs, and *Tg(ptf1a:DsRed)* labels ACs and HCs. HuC/HuD (gray) labels ACs and RGCs. Scale bars: 20 μm.

embryos were found basally at stages at which control HCs have already completed apical migration (Figure 2B). To confirm that the cells stuck in the AC layer were indeed HCs, morphant embryos were stained for the transcription factor Prox1 that labels both HCs and BCs.[45] This staining confirmed that the cells seen in the presumptive AC layer were indeed Prox1-positive basally located HCs (Figures 2A and 2B). Of note, in such AC- and HC-depleted condition, we occasionally observed PRs moving in a multipolar manner, indicating that PRs turn to multipolar migration when instead of ACs and HCs, excess PRs emerge[38] (Figure S1F).

To more directly test how control HCs behave in the absence of surrounding ACs, we used transplantation assays. Different amounts of cells from *Tg(lhx1:GFP); Tg(ptf1a:DsRed)* donor embryos were transplanted into Ptf1a-MO-treated *Tg(lhx1:GFP)* recipient embryos (Figure 2C). When imaging the transplanted embryos at 72 hpf, their retinae had very few ACs or HCs, except for the transplanted cells. Live imaging of these retinae showed that, unlike in controls (Figure 2D; Video S2), transplanted HCs in Ptf1a-MO retinae did not undergo apical migration. Multipolar cell movements now only occurred horizontally within the presumptive AC layer (Figure 2E; Video S2).

By transplanting varying amounts of control cells into the Ptf1a morphants, we asked whether the amount of ACs in the vicinity of HCs influences the efficiency of apical HC migration. In 72 hpf retinae, with only a few transplanted ACs and HCs, HCs remained in the AC layer and did not move toward the PR layer. However, with increasing amounts of transplanted ACs that surrounded HCs, more HCs left the presumptive AC layer. In this case, HCs often laminated below the PRs (Figure 2F). This indicated a relationship between the amount of ACs present in the vicinity of or in contact with HCs and the ability of HCs to initiate multipolar apical movement. Thus, unlike BCs and PRs, surrounding ACs are important for the initiation of HC multipolar apical migration.

Transcriptomic analysis combined with a high-content *in vivo* knockout screen reveals candidate genes instructing horizontal cell migration

A small but consistent number of HCs do not migrate apically when PR layer formation is disrupted (Figures 1F; S1D), and HCs fail to move apically without surrounding ACs (Figure 2F). These observations argue that interactions between HCs and ACs, and possibly also between HCs and PRs, steer multipolar HCs out of the AC layer and toward the PR layer. Previous work showed that neither stiffness gradients nor fibrous ECM-mediated guidance are present within the developing INL.[31] We therefore hypothesized that HC navigation from the basal AC layer to apical positions beneath the PR layer is steered by cell-cell signaling between ACs and HCs and PRs and HCs, respectively.

To identify potential signaling cues, we performed a transcriptome analysis. We dissected retinae from a *Tg(lhx1:GFP); Tg(ptf1a:DsRed)* reporter line at 38 hpf (basal HC movement), 48 hpf (HC enrichment in the AC layer), and 58 hpf (apical HC migration toward PRs)[15] (Figure S1A). Next, we sorted HCs, ACs, and PRs based on lhx1:GFP (for PRs and HCs) and ptf1a:DsRed (for HCs and ACs) reporter expression (Figure 3A). Differential expression analysis (DESeq2; p value < 0.05, log2 fold change > 1) was performed on RNA-seq data from four biological replicates per developmental stage (ENA: PRJEB80557) to identify differentially expressed genes between ACs and HCs and PRs and HCs across stages of HC migration.

To assess candidate gene function on HC migration, we performed an *in vivo* F0 CRISPR screen analyzing over 200 embryos per gene (Figure 3A), similar to the *vsx1+vsx2* and *prdm1a/prdm1b* knockouts (Figures 1D and 1E).[36] To accurately assess the penetrance and phenotypic variability of the knockouts, we employed automated high-content imaging of 72 hpf F0 KO embryos using specialized 96-well plates with uniform embryo alignment.

The *onecut1* gene, known to be involved in HC differentiation in mouse and chick, served as a positive control.[46–48] As expected, *onecut1* showed high expression in HCs in the transcriptomic analysis at all developmental stages, most prominently at 38 hpf (Figure S2A). Targeting three different *onecut1* loci in the *Tg(lhx1:GFP* [PRs, HCs]*; ptf1a:DsRed* [ACs, HCs]) reporter line, we found that, similar to *Onecut1*$^{-/-}$ mice,[46,47] *onecut1* KO zebrafish larvae showed no or very few HCs at 72 hpf, whereas retinal lamination appeared otherwise comparable to the *scrambled* KO controls (Figure S2B). As HC migration occurs independently of fibrous ECM, mechanosensing or integrin-based signaling,[31] we focused on genes upregulated in HCs and associated with non-fibrous ECM components or cell-cell adhesion by manually screening candidates from the DESeg2-filtered dataset (Table S1).

F0 KO embryos in these categories showed phenotypes ranging from no discernible differences to controls to partial HC retention in the AC layer. The latter included genes encoding protocadherin 8 (*pcdh8*), protocadherin γ cluster (*pcdh-γ*), and DS cell adhesion molecule like 1 (*dscaml1*; Figure S5). Other F0 KOs, for example for the ECM glycoproteins tenascin C (*tnc*) or tenascin R (*tnr*), affected overall retinal lamination. This initial screen demonstrated that coupling transcriptomics analysis with an F0 KO screening platform can extract functionally relevant candidates. It also provided some insights into possible HC self-avoidance[49,50] and a role for non-fibrous ECM in retinal lamination. However, this approach alone was insufficient to identify specific cell-cell signaling mechanisms between HCs, ACs, and PRs. Therefore, we generated a pipeline to specifically screen signaling-related targets.

NATMI analysis uncovers specific repulsive and attractive ligand-receptor interactions for horizontal cell migration

To identify secreted or contact-dependent ligands from ACs or PRs that interact with HC-expressed receptors, we analyzed expression changes between 38–48 hpf and 48–58 hpf time points using the NATMI toolkit. This toolkit predicts cell-cell communication networks using a database (connectome) of 2,293 ligand-receptor pairs, curated based on published studies.[51] As the original connectome was based on mouse and human datasets, we created a zebrafish connectome using NCBI HomoloGene and ZFIN orthology datasets, with help of the authors[51] (Table S1). Results of this analysis were inspected for

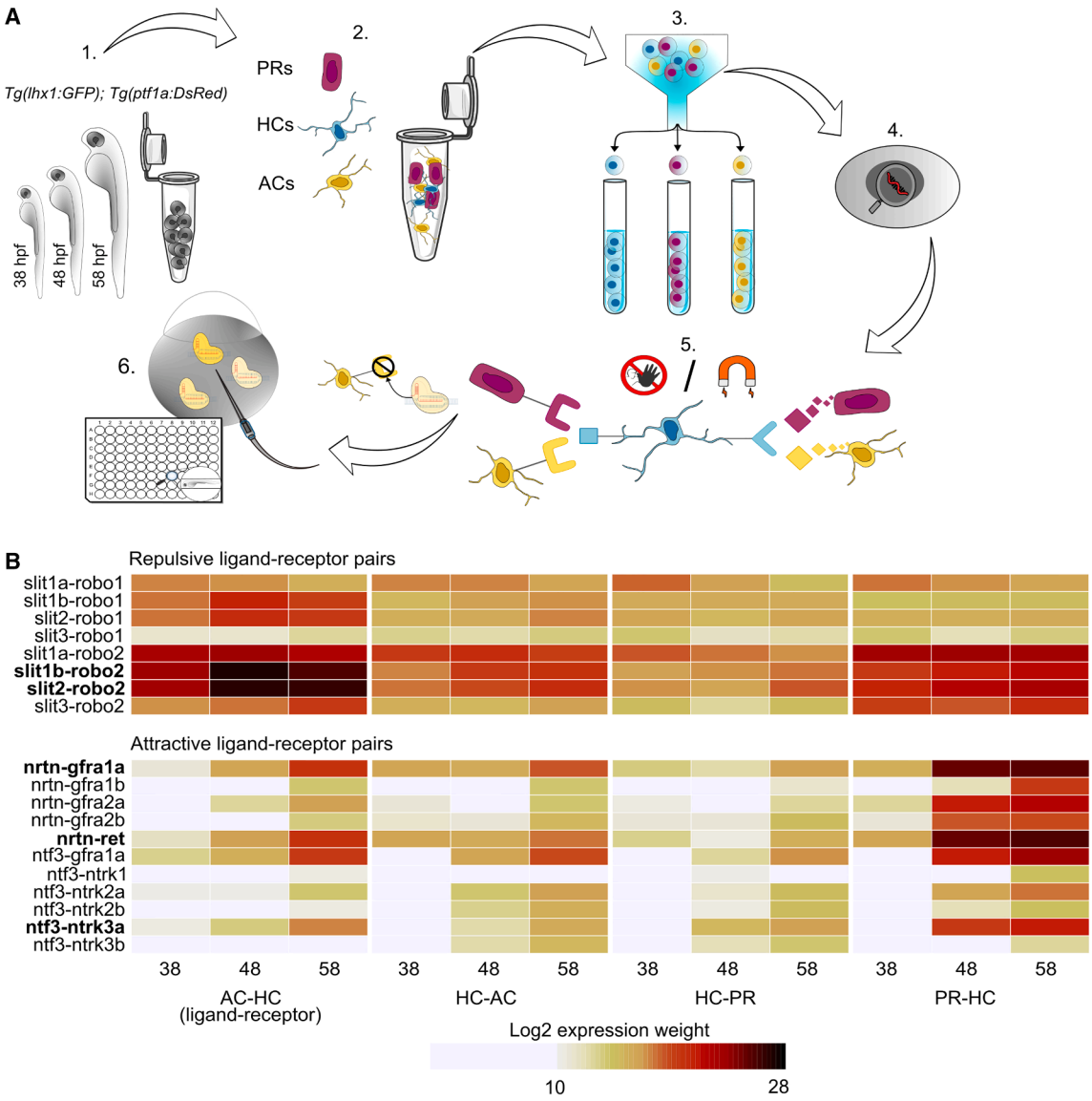

Figure 3. Transcriptomic profiling combined with high-content knockout screen identify candidates guiding HC navigation

(A) Experimental pipeline to extract ligand-receptor based guidance cues in horizontal cell migration. Retinae from *Tg(lhx1:GFP [PRs, HCs]); Tg(ptf1a:DsRed [ACs, HCs])* embryos at 38, 48, and 58 hpf (1.) were dissociated (2.) and FACS-sorted (3.). The derived RNAseq data (4.) was analyzed with zebrafish-adapted NATMI (5.). Shortlisted candidates were tested by high-throughput *in vivo* CRISPR screening (6.).

(B) Heatmap of NATMI-predicted repulsive and attractive ligand-receptor interactions (log2 mean-expression weight) between HCs and ACs or PRs across three developmental stages. In AC-HC, HC-AC, HC-PR, and PR-HC columns, the first nominator is for the specific ligand and the second for the corresponding receptor expressed in that cell type. Ligand-receptor pairs with the strongest temporal or cell-type-specific changes are highlighted in bold.

See Figure S2D and Table S1.

repulsive and attractive ligand-receptor pairs (Table S1). Analysis of filtered expression-weight heatmaps (log2 multiplied expression of average ligand and receptor counts[51]) identified Slit1b-Robo2 and Slit2-Robo2 as prominent repulsive ligand-receptor pairs between ACs (ligand) and HCs (receptor; Figures 3B and S2C). Both *slit1b/slit2* and *robo2* expressions peaked at the 48 hpf, matching the onset of HC apical migration. In contrast, *slit3*, *slit1a*, or *robo1*, known to drive Slit-mediated repulsion in axon guidance,[52–54] showed no notable expression or no upregulation (Figures 3B; Table S1), indicating specificity of the identified pairs. Semaphorin 3 class ligands (Sema3aa and Sema3fb) also emerged as potential repulsive candidates[55,56] but showed weaker expression-weight differences (Figure S2D), and their F0 KO produced only mild HC retention phenotypes (Figures S2D and S5). Thus, they were not analyzed further.

NATMI analysis of PRs (ligand) and HCs (receptor) interactions revealed glial cell line-derived neurotrophic factor (GDNF) family member neurturin (*nrtn*), Gfrα1a and Gfrα-associated Ret

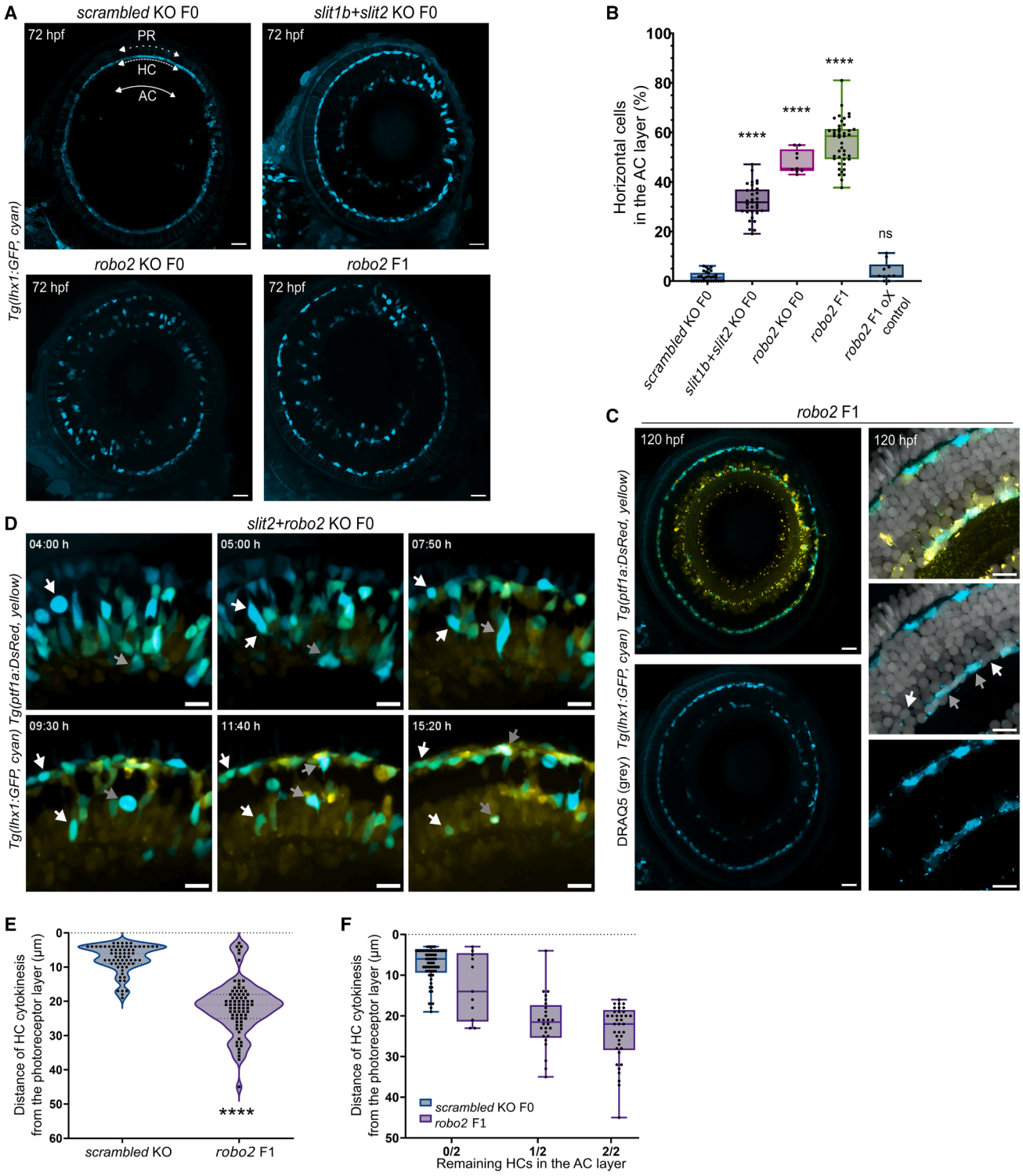

Figure 4. Slit-Robo signaling is required for HC exit from the amacrine cell layer

(A) 72 hpf retinae from *scrambled*, *slit1b+slit2* F0, and *robo2* F0 as well as *robo2* F1 KO embryos. In *scrambled* KO, HCs (cyan) laminate beneath the PR layer (dotted line with arrows), forming the HC layer (dense dotted line with arrows). In *slit1b+slit2* or *robo2* KOs, HCs remain within the AC layer (white line with arrows). *Robo2* F1 mutants phenocopy *robo2* F0. *Tg(lhx1:GFP)* labels the HCs. Scale bars: 20 µm. See Figure S3E.

(B) Quantification of HCs remaining in the AC layer (>5 µm from PRs) in *scrambled*, *slit1b+slit2*, and *robo2* KO and *robo2* F1, as well as in *robo2* F1 outcross with wild-type control. *N* = 31 (*scrambled*), 33 (*slit1b+slit2*), 9 (*robo2* F0), 43 (*robo2* F1), and 10 (*robo2* F1 oX). See Figure 1F. *p* values (Mann-Whitney test vs. *scrambled*

(legend continued on next page)

receptors,[57] as well as neurotrophin-3 (NT-3; *ntf3*) and the Ntrk3a receptor,[58] as prominent candidate signaling pairs (Figure 3B). To date, NT-3 and GDNF family members have been mainly studied in the context of cell migration in peripheral nervous system development, with neurturin additionally reported as a potential protective factor for neurodegenerative disorders.[59–63] Like *slit1b* and *slit2* in ACs, *nrtn* and *ntf3* expression peaked at 48 hpf in PRs. Concurrently, their corresponding receptors *gfra1a*, *ret*, and *ntrk3a* also reached peak expression levels in HCs.

Together, the zebrafish-optimized NATMI analysis enabled extraction of candidate repulsive signals between ACs and HCs and attractive ligand-receptor pairs between PRs and HCs for functional testing using the F0 CRISPR screen.

Slit1b/Slit2 and Robo2 are involved in horizontal cell demixing from the amacrine cell layer

Slits instruct axon guidance by repelling Robo-expressing neuronal growth cones in both invertebrates and vertebrates.[64–66] During axon guidance in the developing retina, Slit1/2-Robo2 pairs are important cues for directing RGC axons toward the brain.[67–69] Further, Slit-Robo signaling also guides non-neuronal cell types such as neural crest cells and leukocytes.[70,71] However, to the best of our knowledge, a direct involvement of Slit1/2-Robo2 signaling in neuronal migration has not been shown so far.

Based on our NATMI analysis, Slit1b and Slit2 upregulation in ACs coincided with increased Robo2 expression in HCs during their exit from the AC layer[15,24] (Figures 3B and S1A). To confirm this expression pattern, we performed *in situ* hybridization for Slit2 and Robo2 mRNA using whole-mount and sectioned embryos (Figures S3A and S3B). At 38 hpf, Slit2 mRNA signal was mainly detected in the ciliary marginal zone and faintly in the optic nerve. From 48 hpf onwards, AC layer-specific Slit2 expression increased, as seen previously.[68,69] Consistent with its role in RGC axon guidance, Slit2 mRNA localized around optic nerve axons but not within the RGC layer.[69] Robo2 mRNA was absent at 38 hpf but appeared in the RGC and AC layers at 48 hpf, as previously reported (Figure S3B).[72,73] At 58 hpf, Robo2 signal was seen in the RGC layer and within the INL, including the HC cell layer, reflecting published data.[68] Negative control sense probes for Slit2 and Robo2 showed no signal (Figures S3A and S3B).

Migrating cells use protrusions to probe their environment and sense signaling cues like Slit2, at least *in vitro*.[74–76] As migrating HCs extend multiple protrusions,[31,77] we asked whether the Robo2 receptor localizes there. Antibody staining showed Robo2 protein at the plasma membrane and within HC protrusions (Figure S3C). Live imaging of a UAS:Robo2-mCherry in the *Tg(ptf1a:Gal4; UAS:gap-YFP* [ACs, HCs]) reporter line further revealed dynamic Robo2 puncta within HC protrusions (Figure S3D and Video S3).

Based on these data, we probed whether Slit-Robo signaling regulates apical HC migration. We generated F0 KO embryos targeting both *slit1b* and *slit2*, *robo2*, or a combination of *slits+ robo2* together (Figures 4A, S3E, and S3F) and performed an *in vivo* screen for these KOs as described above (Figures 3A and S2A). Knockout of either Slit1b/Slit2 or the Robo2 receptor caused a large fraction of HCs to remain in the AC layer at 72 hpf, compared to *scrambled* KO controls (Figure 4B). Targeting Robo2 mRNA with a validated splice-blocking MO[78] recapitulated the *robo2* F0 KO phenotype (Figure S3G).

To confirm the specificity of the effect, we generated *robo2* F1 mutants carrying premature stop codons (Table S1). Retinae of Robo2 mutant embryos displayed similar numbers of HCs remaining in the AC layer as the *robo2* F0 KOs (Figures 4A, 4B, and S3E). This phenotype was lost when introducing a functional copy of the gene.

Since Slit1b/Slit2 work through Robo2, and Robo2 loss caused the strongest phenotype with around half of the HCs failing to laminate beneath the PR cell layer (Figure 4B), we focused subsequent analyses on Robo2. In Robo2 mutants, similar numbers of ectopically placed HCs were observed at 72 hpf and 5 days post fertilization (dpf; Figures 4A and 4C), suggesting that misplaced HCs are not rescued over development and do not undergo apoptosis.

We conclude that downregulation of Slit1b/2-Robo2 impairs the apical migration of roughly half of all HCs. This indicates that repulsive Slit-Robo signaling between ACs and HCs, likely sensed through HC protrusions, governs HC departure from the AC layer.

Upon Slit-Robo downregulation, signaling from the photoreceptor cell layer becomes critical for horizontal cell apical arrival

While half of the HCs remain in the AC layer in the Slit1b/2 and Robo2 knockout embryos, the other half still managed to reach the PR layer (Figures 4A, 4C, and S1A). HC morphology in control- vs. KO embryos was similar, suggesting that the correctly laminating HCs migrate like controls. Each HC undergoes a

KO) = <0.0001 (*slit1b+slit2* ^****); <0.0001 (*robo2* F0 ****), <0.0001 (*robo2* F1****), and 0.05 (*robo2* F1 oX wild-type ns). Boxes show interquartile range; center line = median; whiskers = min/max; dots = individual retinae.

(C) Ectopically placed HCs in the AC layer (cyan and yellow) of 5 dpf *robo2* F1 larvae. The lower panel shows Airyscan images of the *robo2* F1 retina. Gray arrows label ectopic HCs (cyan and yellow). HCs (gray arrows) show flattened nuclei compared to round AC nuclei (white arrows). *Tg(ptf1a:dsRed)* labels ACs and HCs; *Tg(lhx1:GFP)* labels HCs and DRAQ5 (gray) labels nuclei. Scale bars: 20 and 10 μm, respectively.

(D) Time-lapse montage of HC (cyan and yellow) migration in a *slit2+robo2* F0 embryo. Two dividing HCs are labeled (white and gray arrows), and their sister cells tracked after division. Scale bars: 5 μm. See Video S3 and Figure S3F.

(E) Division positions of HCs relative to the PR cell layer (μm) in *scrambled* KO (blue) and in *robo2* F1 (purple) embryos. *N* = 67 (*scrambled* KO) and 75 (*robo2 F1*) divisions from 6 *scrambled* and 6 *robo2* F1 embryos. *p* value (Mann-Whitney test) = <0.001****. Dashed line = median, dotted lines = quartiles, dots = individual measurements.

(F) Division positions vs. final laminar outcome of sister HCs in *scrambled* KO (blue) and in *robo2* F1 (purple) embryos; see Figure 4E. 0/2 = both sisters correctly laminate. 2/2 = both remain in the AC layer. *N* = 67 (*scrambled* KO) and 75 (*robo2* F1) division events. Boxes show interquartile range; center line = median; whiskers = min/max; dots = individual retinae.

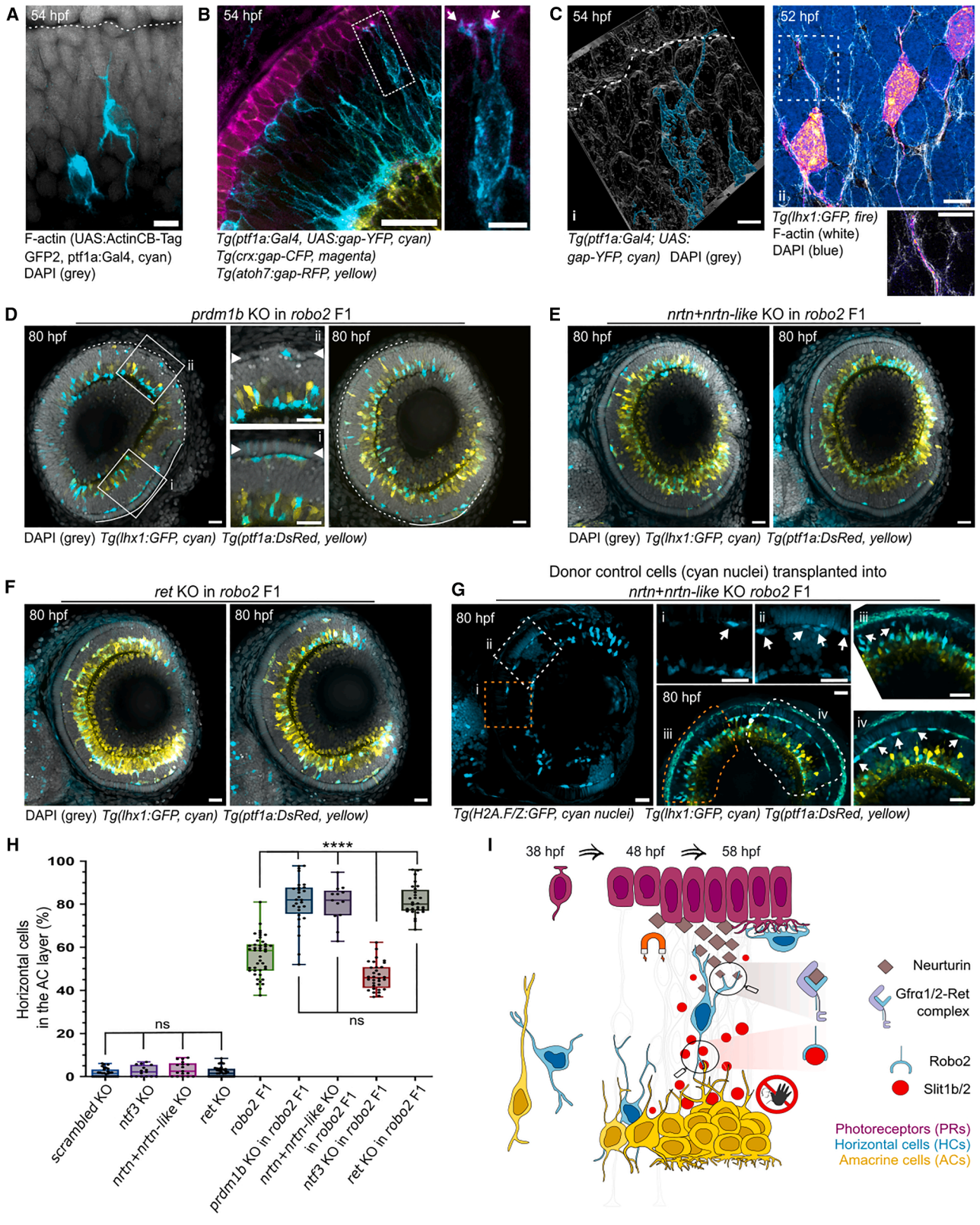

(legend on next page)

terminal division during migration along the INL, mostly close to the PR cell layer.[24] When analyzing HC division positions in *robo2* KO, we noted that, whereas in *scrambled* KO most divisions occurred close to the PR layer, many HCs in the Robo2 mutant embryos divided at more basal positions in the INL (Figure 4E). To probe whether division position correlated with HC lamination success, we performed live imaging of HC sister cells in *slit2+robo2* KO embryos. In *slit2+robo2* KOs, sister HCs that, after division, located closer to the PR layer were more likely to laminate correctly, while HCs remaining at more basal positions after division moved away from the PR layer (Figure 4D; Video S3). In *scrambled* KO controls, both sister cells moved toward and laminated below the PR layer (Video S3). When divisions occurred more basally in the INL (>20 μm from PRs), both sister cells usually failed to migrate apically and stayed within the AC layer (Figure 4F). These observations suggest that while Slit1b/2-Robo2 provides strong apical-directed repulsion, additional cues guide HCs located near the PR layer.

Neurturin provides an attractive signaling cue guiding multipolar horizontal cells toward the photoreceptor cell layer

Knockout of *robo2*, *slit2*, or their combination did not fully disrupt HC apical multipolar migration, and HCs that divided closer to the PR layer were able to laminate correctly (Figures 4A–4F). Further, migrating multipolar HCs frequently extend protrusions toward the PR layer (Video S1), as also seen in the developing mouse retinae.[29,77] This protrusive activity was also observed in *slit2+robo2* KO retinae (Video S3). Given Robo2 localization in HC protrusions (Figures S3C and S3D), we analyzed the protrusive behavior in more detail. In control HCs undergoing multipolar apical migration, protrusions were enriched with F-actin and frequently contacted the PR layer (Figures 5A and 5B). 3D imaging of the retinae of 52–54 hpf *Tg(lhx1:GFP); Tg(ptf1a:DsRed)*, and *Tg(ptf1a:Gal4; UAS:gap-YFP)* reporter lines subjected to expansion microscopy[79,80] further showed that HC protrusions can extend between neighboring cells (Figure 5C) and contact the PR layer (Figure S4A and Video S4). This suggests that HC protrusions sense short-range PR-derived signals.

As partial removal of PRs in *prdm1b* KOs caused a small but reproducible proportion of HCs to remain in the AC layer (Figures 1F; S1D), we speculated that, in addition to Slit-Robo repulsion in the AC layer, an additive instructive signal could come from PRs guiding the last phase of apical HC migration. To test this, we knocked out *prdm1b* in the Robo2 mutant embryos, generating apical patches devoid of PRs (Figure 5D), as seen in *prdm1b* KO (Figure 1E). In this condition, areas showing control-like PRs also showed a similar ratio of HCs still laminating beneath this layer. However, in areas with a compromised PR layer, most of the HCs remained in the AC layer (Figure 5D), indicating a role for PR-derived signaling component(s) in successful HC apical migration. We again consulted our NATMI analysis and removed the two most prominent attractive signaling candidates, neurturin (*nrtn*) and NT-3 (*ntf3*; Figure 3B). For complete neurturin removal (neurturin KO), we jointly targeted *nrtn* and neurturin-like (*nrtn-like/FO834855.1*) (Figure S4B). In control embryos, neither the absence of neurturin nor NT-3 ligands, nor their putative receptors (Gfrα1a, Ret, or Ntrk3a, respectively), had a detectable effect on HC apical migration (Figure S4C). Knocking out the attractive ligand *ntf3* in Robo2 mutants did not show any additive effects (Figures S3E and S4D).

In contrast, neurturin knockout in Robo2 mutants caused a near-complete failure of HC apical migration (Figure 5E). Live imaging of the neurturin KO in Robo2 mutants showed that most HCs only move within the AC layer and do not reach apical

Figure 5. Multipolar horizontal cells use protrusions and navigate along repulsive Slit-Robo and attractive neurturin signaling

(A) Chromobody (CB)-labelled F-actin (UAS:ActinCB-TagGFP2; ptf1a:Gal4, cyan) in apically migrating HCs at 54 hpf. Dashed line marks the PR layer. DAPI (gray) labels nuclei. Scale bar: 5 μm.

(B) Migrating HCs (cyan, magnified white dashed box) with protrusions (white arrows) contacting PRs (magenta) at 54 hpf. *Tg(atoh7:gap-RFP, yellow)*, *Tg(ptf1a:Gal4; UAS:gap-YFP, cyan)*, and *Tg(crx:gap-CFP, magenta)*. Scale bars: 20 and 10 μm respectively. See Figure 1B and Video S1.

(C) Expansion microscopy of HC (*Tg(ptf1a:Gal4; UAS:gap-YFP)* protrusions. (i) 3D rendering showing an HC (cyan) protrusion touching the PR layer (white dashed line). (ii) HCs (fire) migrating between neighboring cells with a protrusion (magnification of boxed area) extending between two cells labeled with F-actin (white). Nuclei stained with DAPI (gray/blue). Scale bars: 20 μm. See Video S4 and Figure S4A.

(D) *prdm1b* KO in a *robo2* F1 background at 80 hpf. Areas with a more intact PR layer (solid line; i) reproduce the *robo2* KO phenotype, whereas areas with absent or abnormal PR layer (dashed line; ii) show enhanced HC retention in the AC layer. Magnified areas (white boxes; i/ii); PR cell layer (white arrowheads). *Tg(ptf1a:DsRed, yellow)* labels ACs and HCs, and *Tg(lhx1:GFP, cyan)* labels HCs. DAPI (gray) marks nuclei. Scale bars: 20 μm. See Figure 1E.

(E) Neurturin (*nrtn+nrtn-like*) KO in a *robo2* F1 causes near-complete HC (cyan and yellow) retention in the AC layer (yellow) at 80 hpf. Other retinal layers are similar to controls. DAPI (gray) marks nuclei. Scale bars: 20 μm. See Figures S4B, S4C, and S4E and Video S4.

(F) *Ret* KO in *robo2* F1 phenocopies neurturin depletion, causing most HCs (cyan and yellow) to remain in the AC layer (yellow) at 80 hpf. Nuclei were stained with DAPI (gray). Scale bars: 20 μm. See Figure S4C.

(G) Transplantation of control cells *Tg(H2A.F/Z:GFP, cyan nuclei)* into neurturin KO *robo2* F1 *Tg(lhx1:GFP, cyan), Tg(ptf1a:DsRed, yellow)*. Around areas with control cells (ii and iv, magnified from white boxes), more Robo2-lacking recipient HCs (cyan and yellow) reach control PRs (white arrows), compared to areas without donor cells (i and iii, magnified from orange boxes). Scale bars: 20 μm. See Figures 2C and S4F.

(H) Quantification of HCs remaining in the AC layer (>5 μm away from PRs) after the depletion of attractive cues alone or combined with Robo2 loss. $N = 31$ (*scrambled* KO), 15 (*ntf3* KO), 17 (*nrtn+nrtn-like* KO), 33 (*ret* KO), 43 (*robo2* F1), 13 (*prdm1b* KO in Robo2 F1), 28 (*nrtn+nrtn-like* KO in *robo2* F1), 32 (*ntf3* KO in Robo2 F1), and 28 (*ret* KO in Robo2 F1). p values (Mann-Whitney test) = 0.3531 (*ntf3* KO vs. *scrambled* KO) ns, 0.0684 (*nrtn+nrtn-like* KO vs. *scrambled* KO) ns, 0.4805 (*ret* KO vs. *scrambled* KO) ns, <0.0001 (*prdm1b* KO in *robo2* F1 vs. *robo2* F1) ****<0.0001 (*nrtn+nrtn-like* KO in *robo2* F1 vs. *robo2* F1) ****<0.0001 (*ntf3* KO in *robo2* F1 vs. *robo2* F1) ****<0.0001 (*ret* KO in *robo2* F1 vs. *robo2* F1) ****0.7037 (*prdm1b* KO vs. *nrtn+nrtn-like* KO in *robo2* F1) ns, and 0.9835 (*prdm1b* KO vs. *ret* KO in *robo2* F1) ns. Boxes show interquartile range; center line = median; whiskers = min/max; dots = individual retinae.

(I) Schematic of guidance cues coordinating multipolar HC navigation. At 48 hpf, ACs start to express Slit1b and Slit2 to repulse Robo2 expressing HCs toward the PRs. Concurrently, PRs initiate the expression of secreted neurturin to further attract HCs positive for the Gfrα1/2-Ret receptor complex toward the PR layer.

positions (Video S4). A similar phenotype was observed when neurturin and neurturin-like were depleted through morpholino approaches in the Robo2 mutants (Figure S4E). Knockout of neurturin receptors GFRα1a+GFRα1b did not show enhanced HC displacement in the Robo2 mutant background (Figure S4D). This likely reflects compensation by other GFRα family members, particularly GFRα2, which also binds neurturin.[81] However, knockout of the Ret kinase, a co-receptor for Gfrα family proteins,[81] in Robo2 mutants resulted in a phenotype comparable to that observed upon neurturin knockout in Robo2 mutants (Figure 5F). In control background, Ret removal had no discernible effect on HC lamination (Figure S4C).

To more directly test if PRs are the source of attractive neurturin, we transplanted *Tg(H2A.F/Z:GFP*, nuclei) control cells into neurturin F0 KO in Robo2 mutants. When the Robo2-deficient recipient HCs (unresponsive to AC-derived Slits) were surrounded by control cells, including PRs, HCs were more successful in reaching the PR cell layer (Figures 5G; S4F), similar to what is observed in Robo2 mutants when neurturin is present (Figure 4A). These observations support a model in which PR-derived neurturin promotes HC migration toward the PR layer.

Quantifying the HCs remaining in the AC layer in response to these KOs provided further evidence that while depleting PRs, neurturin, or its co-receptor Ret in control embryos had little effect on HC navigation in controls, in embryos lacking Robo2, these factors become critical to steer HC apical migration close to the apical PRs (Figure 5H).

Taken together, we propose that Slit1b/2-Robo2 signaling between ACs and HCs at 48 hpf provides strong apical-directed repulsion for HCs to leave the AC layer. Concurrently, PR-derived neurturin attracts HCs through Gfrα1/2-Ret receptors (Figure 5I). The coordinated action of spatially distinct yet concurrently upregulated repulsive and attractive cues thus steer multipolar HC migration in the developing vertebrate retina.

DISCUSSION

Multipolar neuronal migration is an evolutionary conserved, yet still poorly understood mode of cell movement in the developing central nervous system. Here, we investigated this migration mode in the zebrafish retina, focusing on HC lamination. By combining transcriptomics, high-content *in vivo* knockout screens and high-resolution *in vivo* imaging, we reveal repulsive and attractive cues that collectively ensure robust HC positioning. HC migration is only mildly affected by a disorganized PR layer or the absence of BCs. However, loss of the neighboring ACs at stages when both cell types occupy the INL obstructs HC apical migration toward the PRs.

Our knockout experiments further show that HC apical movement depends on AC-expressed repulsive Slit1b/2 ligands, sensed by Robo2 receptors on HCs. After exiting the AC layer, PR-derived neurturin further promotes HC guidance toward the PR cell layer through Gfrα1/2-Ret receptors in HCs. Although weaker than Slit-Robo signaling, neurturin becomes critical when repulsive cues are compromised. Together, combined cell depletion, knockout, and transplantation experiments strongly support a model in which multipolar migration is guided by extrinsic signals from neighboring cells rather than by fixed cellular scaffolds, a principle likely conserved across the developing nervous system.

Previous work in the rodent neocortex has suggested that multipolar migration represents a transient, permissive "waiting lounge phase" preceding bipolar migration.[10,11,13,82] However, our data argue that this might be a reductionist view. In the developing zebrafish retina, multipolar HCs display dynamic space adaptation to navigate densely packed tissue and successfully laminate even after removal of specific neuronal populations or increased tissue stiffness.[24,31] Moreover, several retinal neurons, including RGCs[25] and PRs (this study), can switch to multipolar migration modes when their canonical bipolar migration is compromised, indicating that this mode of migration provides an alternative strategy under crowded or perturbed conditions. Based on these findings, we propose that multipolar migration serves as a robust and adaptive mechanism for neuronal positioning, particularly when other ways of movement become less efficient. A better understanding of the capacity and constraints of multipolar migration in different brain regions will be important to provide insight into neurodevelopmental disorders caused by impaired suspension of the multipolar migration phase.[5]

HC multipolar migration operates efficiently and independently of fibrous ECM or stiffness gradients,[31] instead of relying on spatially distributed guidance cues. Loss of ACs produced the strongest HC basal retention phenotype, comparable only to combined disruption of Slit1b/2-Robo2 and neurturin-Gfrα1/2-Ret signaling. This suggests that additional mechanisms further contribute to HC-AC demixing, potentially involving differences in cortical tension or cell-cell adhesion.[83] Indeed, interference with Protocadherin 8, a family member of cell-adhesion molecules that function as cellular fingerprints to define self from non-self,[50] caused subtle but persistent HC positioning defects (Figure S5), pointing to a possible role for protocadherin-mediated adhesion in fine-tuning lamination. Further studies should thus investigate the contribution of mechanical properties and/or protocadherin adhesion patterns in robust and precise HC positioning.

Out of the two extrinsic, secreted cues that steer HC migration, Slit1b/2 binding to Robo2 acts as a repulsive axis sufficient to drive the HCs out of the AC layer. While several Slit-Robo interactions have been studied in neurodevelopment, particularly during axon guidance,[84] these molecules have not yet been prominently shown to be involved in guiding neuronal lamination *in vivo*. Our findings therefore add to the expanding repertoire of Robo-mediated processes in neurodevelopment[54,66,70] and demonstrate a direct Slit-Robo interaction guiding neuronal migration *in vivo*.

The apical movement of HCs is further supported by PR-derived neurturin attraction sensed through Gfrα1/2 receptors and Ret kinase[85,86] in HCs. While neurturin cannot fully rescue HC apical migration when the Slit-Robo axis is impaired, its presence enhances the robustness of successful HC navigation. Consistent with our findings, Gfrα1-Ret are also expressed in chick and mouse retinae,[87,88] and neurturin-deficient mice display an abnormal outer plexiform layer with atypical HC axons,[87] indicating that neurturin may similarly influence HC migration in other systems.

Taken together, the spatiotemporal interplay of Slit1b/2-Robo2 and neurturin-Gfrα1/2-Ret signaling highlights how multipolar migration can be efficiently orchestrated through the integration of spatially distinct extrinsic cues. Combined action of multiple localized cues thus extends the effectiveness of multipolar migration and thereby allows it to operate reliably even within packed tissue environments.

During vertebrate retinal development, the lamination process of five retinal layers largely overlap, unlike the sequential inside-out mechanism in the developing mammalian neocortex.[2] This potentially requires a broader spectrum of migration modes including somal translocation in one or two directions as well as multipolar migration that can be uni- or bidirectional. Multipolar migration in addition to being the main module of migration for HCs, most likely also allows other retinal neurons like ACs, RGCs,[25] and PRs to fine-tune their positioning within the crowded, yet dynamic, tissue.[32,33]

Interestingly, the development of reptile or avian cortex brain areas does not follow the inside-out lamination pattern, showing a high prevalence of multipolar migration.[16,18] This argues that whereas bipolar migratory modes are likely important to enable inside-out type layering, multipolar migration can enhance the robustness of neural tissue patterning through a greater freedom of movement and spatial adaptability controlled by the spatiotemporal orchestration of guidance cues.

Limitations of the study

While our data support a model in which Slit1b/2-Robo2 (AC-HC) and neurturin-Gfrα1/2-Ret (PR-HC) signaling coordinate HC positioning, the *in vivo* nature of our approach imposes limitations. Although essential for capturing migration dynamics and spatially integrated cues in the developing retina, this approach restricts the range of perturbations and molecular resolution that can be achieved. Because cell-type-specific manipulations of ACs and HCs are not feasible in zebrafish, we could not directly test how individual cell populations respond to the loss of specific signaling components. While repulsive and attractive interactions were inferred from expression patterns and functional necessity, protrusion-mediated cell-cell contacts remained below the resolution of live imaging. Fixed and expansion microscopy nevertheless suggest that such protrusions contribute to HC fine positioning at the PR layer.

Together, these limitations highlight key technical challenges and motivate future experiments aimed at testing ligand sufficiency, receptor specificity, and the directional nature of the guidance mechanisms involved.

RESOURCE AVAILABILITY

Lead contact

Requests for further information and resources should be directed to the lead contact, Caren Norden (caren.norden@gimm.pt).

Materials availability

- The Robo2 mutant *Tg(lhx1:GFP); Tg(ptf1a:dsRed)* transgenic line is available from the lead contact upon request.
- For plasmids generated in this study, UAS:ActinCB-TagGFP2 availability is restricted due to MTA for Actin Chromobody (CB) with ChromoTek. Tol2-UAS:Robo2-mCherry is available from the lead contact upon request.

Data and code availability

- RNAseq data have been deposited at the European Nucleotide Archive (ENA), PRJEB80557, and are publicly available as of the date of publication.
- Original microscopy data reported in this paper will be shared by the lead contact upon request.
- Any additional information required to reanalyze the data reported in this paper is available from the lead contact upon request.

ACKNOWLEDGMENTS

We thank all members of the Cell Biology of Tissue Morphogenesis laboratory for lively project discussion. João Coelho, Renata Cunha, and Ricardo Ribeiro gave cloning support, and Mariana Gil helped with transplantation. We acknowledge the Flow cytometry, Bioimaging, Genomic, Bioinformatics, Histopathology, and Aquatic facilities at the Gulbenkian Institute for Molecular Medicine (GIMM, formerly IGC) for technical support. We further thank Rui Hou and Allistair Forest for assistance with updating the NATMI connectome for zebrafish. Guillaume Jacquemet and Julien Vermot are thanked for constructive comments on the manuscript. We are grateful to Eyleen Goh, Jan Kaslin, and Paolo Panza for sharing the pCS2-Robo2, pDEST-ptf1a:Gal4, and UAS:ActinCB-TagGFP2 constructs, respectively. C.N. discloses support for the research of this work from European Research Council consolidator grant (H2020 ERC-2018-CoG-81904). J.I.L. was additionally supported for the research of this work from a Fundação para a Ciência e a Tecnologia CEEC (2023.07063.CEECIND/CP2854/CT0002). R.H. and M.D.R. were supported by the ERC under the European Union's Horizon 2020 research and innovation program (grant agreement no. 101001332) (to R.H.).

AUTHOR CONTRIBUTIONS

Conceptualization, J.I.L., M.D.R., R.H., C.N.; methodology, J.I.L., J.L., M.D.R., E.N., M.R.C.; investigation, J.I.L., M.D.R., M.R.C.; writing – original draft, J.I.L., J.L., M.D.R., R.H., C.N.; writing – review & editing, J.I.L., M.R.C., C.N.; funding acquisition, J.I.L. and C.N.; resources, R.H. and C.N.; supervision, C.N.

DECLARATION OF INTERESTS

The authors declare no competing interests.

DECLARATION OF GENERATIVE AI AND AI-ASSISTED TECHNOLOGIES IN THE WRITING PROCESS

During finalizing the manuscript, the authors used GPT-5 (OpenAI) as a writing aid. The authors edited and validated all the text sections after using the tool and take full responsibility for the content of the publication.

STAR★METHODS

Detailed methods are provided in the online version of this paper and include the following:

- KEY RESOURCES TABLE
- EXPERIMENTAL MODEL
  - Zebrafish husbandry
  - Zebrafish transgenic lines
- METHOD DETAILS
  - DNA constructs and cloning
  - DNA and morpholino injections of zebrafish embryos
  - Whole-mount immunofluorescence staining of zebrafish embryos
  - Retinae dissection and flow cytometry-based sorting of photoreceptor- amacrine- and horizontal cells
  - RNA sequencing and data processing
  - NATMI analysis

- Blastomere transplantation of Ptf1a depleted embryos
- *In vivo* F0 CRISPR guide RNA design and screen
- Robo2 F1 line generation and gDNA sequencing
- Expansion microscopy of the whole zebrafish larvae
- *In situ* hybridization of whole mount embryos and retinal sections
- Spinning disk live-imaging of zebrafish embryos
- Airyscan confocal scan of whole-mount zebrafish retinae
- Image processing and analysis

- QUANTIFICATION AND STATISTICAL ANALYSIS
  - Quantitative analysis of HCs in the AC-layer in different F0 knockouts
  - Analysis of HC cytokinesis positions
  - Statistical analysis and reproducibility

SUPPLEMENTAL INFORMATION

Supplemental information can be found online at https://doi.org/10.1016/j.celrep.2026.116948.

Received: July 31, 2025
Revised: December 22, 2025
Accepted: January 8, 2026
Published: February 3, 2026

REFERENCES

1. Maeda, N. (2015). Proteoglycans and neuronal migration in the cerebral cortex during development and disease. Front. Neurosci. *9*, 98. https://doi.org/10.3389/fnins.2015.00098.
2. Marin, O., Valiente, M., Ge, X., and Tsai, L.-H. (2010). Guiding Neuronal Cell Migrations. Cold Spring Harb. Perspect. Biol. *2*, a001834. https://doi.org/10.1101/cshperspect.a001834.
3. van Battum, E.Y., van den Munkhof, M.H., and Pasterkamp, R.J. (2025). Novel insights into the regulation of neuron migration by axon guidance proteins. Curr. Opin. Neurobiol. *92*, 103012. https://doi.org/10.1016/j.conb.2025.103012.
4. D'Arcangelo, G., Miao, G.G., Chen, S.C., Soares, H.D., Morgan, J.I., and Curran, T. (1995). A protein related to extracellular matrix proteins deleted in the mouse mutant reeler. Nature *374*, 719–723. https://doi.org/10.1038/374719a0.
5. Francis, F., and Cappello, S. (2021). Neuronal migration and disorders – an update. Curr. Opin. Neurobiol. *66*, 57–68. https://doi.org/10.1016/J.CONB.2020.10.002.
6. LoTurco, J.J., and Bai, J. (2006). The multipolar stage and disruptions in neuronal migration. Trends Neurosci. *29*, 407–413. https://doi.org/10.1016/J.TINS.2006.05.006.
7. Ayala, R., Shu, T., and Tsai, L.-H. (2007). Trekking across the Brain: The Journey of Neuronal Migration. Cell *128*, 29–43. https://doi.org/10.1016/j.cell.2006.12.021.
8. Marín, O. (2013). Cellular and molecular mechanisms controlling the migration of neocortical interneurons. Eur. J. Neurosci. *38*, 2019–2029. https://doi.org/10.1111/ejn.12225.
9. Barber, M., and Pierani, A. (2016). Tangential migration of glutamatergic neurons and cortical patterning during development: Lessons from Cajal-Retzius cells. Dev. Neurobiol. *76*, 847–881. https://doi.org/10.1002/dneu.22363.
10. Tabata, H., and Nakajima, K. (2003). Multipolar Migration: The Third Mode of Radial Neuronal Migration in the Developing Cerebral Cortex. J. Neurosci. *23*, 9996–10001. https://doi.org/10.1523/jneurosci.23-31-09996.2003.
11. Tanaka, D.H., Yanagida, M., Zhu, Y., Mikami, S., Nagasawa, T., Miyazaki, J.I., Yanagawa, Y., Obata, K., and Murakami, F. (2009). Random walk behavior of migrating cortical interneurons in the marginal zone: Time-lapse analysis in flat-mount cortex. J. Neurosci. *29*, 1300–1311. https://doi.org/10.1523/JNEUROSCI.5446-08.2009.
12. Noctor, S.C., Martínez-Cerdeño, V., Ivic, L., and Kriegstein, A.R. (2004). Cortical neurons arise in symmetric and asymmetric division zones and migrate through specific phases. Nat. Neurosci. *7*, 136–144. https://doi.org/10.1038/nn1172.
13. Namba, T., Shinohara, H., and Seki, T. (2019). Non-radial tortuous migration with cell polarity alterations of newly generated granule neurons in the neonatal rat dentate gyrus. Brain Struct. Funct. *224*, 3247–3262. https://doi.org/10.1007/S00429-019-01971-0.
14. Kitazawa, A., Kubo, K.i., Hayashi, K., Matsunaga, Y., Ishii, K., and Nakajima, K. (2014). Hippocampal Pyramidal Neurons Switch from a Multipolar Migration Mode to a Novel "Climbing" Migration Mode during Development. J. Neurosci. *34*, 1115–1126. https://doi.org/10.1523/JNEUROSCI.2254-13.2014.
15. Chow, R.W., Almeida, A.D., Randlett, O., Norden, C., and Harris, W.A. (2015). Inhibitory neuron migration and IPL formation in the developing zebrafish retina. Dev. Camb. *142*, 2665–2677. https://doi.org/10.1242/dev.122473.
16. Scott, B.B., Gardner, T., Ji, N., Fee, M.S., and Lois, C. (2012). Wandering Neuronal Migration in the Postnatal Vertebrate Forebrain. J. Neurosci. *32*, 1436–1446. https://doi.org/10.1523/JNEUROSCI.2145-11.2012.
17. Martínez-Martínez, M.Á., Ciceri, G., Espinós, A., Fernández, V., Marín, O., and Borrell, V. (2019). Extensive branching of radially-migrating neurons in the mammalian cerebral cortex. J. Comp. Neurol. *527*, 1558–1576. https://doi.org/10.1002/cne.24597.
18. Nomura, T., Ohtaka-Maruyama, C., Kiyonari, H., Gotoh, H., and Ono, K. (2020). Changes in Wnt-Dependent Neuronal Morphology Underlie the Anatomical Diversification of Neocortical Homologs in Amniotes. Cell Rep. *31*, 107592. https://doi.org/10.1016/j.celrep.2020.107592.
19. Baden, T. (2024). The vertebrate retina: a window into the evolution of computation in the brain. Curr. Opin. Behav. Sci. *57*. https://doi.org/10.1016/j.cobeha.2024.101391.
20. Hahn, J., Monavarfeshani, A., Qiao, M., Kao, A.H., Kölsch, Y., Kumar, A., Kunze, V.P., Rasys, A.M., Richardson, R., Wekselblatt, J.B., et al. (2023). Evolution of neuronal cell classes and types in the vertebrate retina. Nature *624*, 415–424. https://doi.org/10.1038/s41586-023-06638-9.
21. Cowan, C.S., Renner, M., De Gennaro, M., Gross-Scherf, B., Goldblum, D., Hou, Y., Munz, M., Rodrigues, T.M., Krol, J., Szikra, T., et al. (2020). Cell Types of the Human Retina and Its Organoids at Single-Cell Resolution. Cell *182*, 1623–1640.e34. https://doi.org/10.1016/J.CELL.2020.08.013.
22. Soucy, J.R., Todd, L., Kriukov, E., Phay, M., Malechka, V.V., Rivera, J.D., Reh, T.A., and Baranov, P. (2023). Controlling donor and newborn neuron migration and maturation in the eye through microenvironment engineering. Proc. Natl. Acad. Sci. USA *120*, e2302089120. https://doi.org/10.1073/pnas.2302089120.
23. Kozlowski, C., Hadyniak, S.E., and Kay, J.N. (2024). Retinal neurons establish mosaic patterning by excluding homotypic somata from their dendritic territories. Cell Rep. *43*, 114615. https://doi.org/10.1016/j.celrep.2024.114615.
24. Amini, R., Labudina, A.A., and Norden, C. (2019). Stochastic single cell migration leads to robust horizontal cell layer formation in the vertebrate retina. Development *146*, dev173450. https://doi.org/10.1242/dev.173450.
25. Icha, J., Kunath, C., Rocha-Martins, M., and Norden, C. (2016). Independent modes of ganglion cell translocation ensure correct lamination of the zebrafish retina. J. Cell Biol. *215*, 259–275. https://doi.org/10.1083/jcb.201604095.
26. Edqvist, P.H.D., and Hallböök, F. (2004). Newborn horizontal cells migrate bi-directionally across the neuroepithelium during retinal development. Development *131*, 1343–1351. https://doi.org/10.1242/dev.01018.

27. Capowski, E.E., Samimi, K., Mayerl, S.J., Phillips, M.J., Pinilla, I., Howden, S.E., Saha, J., Jansen, A.D., Edwards, K.L., Jager, L.D., et al. (2019). Reproducibility and staging of 3D human retinal organoids across multiple pluripotent stem cell lines. Dev. Camb. *146*, dev171686. https://doi.org/10.1242/dev.171686.

28. Sridhar, A., Hoshino, A., Finkbeiner, C.R., Chitsazan, A., Dai, L., Haugan, A.K., Eschenbacher, K.M., Jackson, D.L., Trapnell, C., Bermingham-McDonogh, O., et al. (2020). Single-Cell Transcriptomic Comparison of Human Fetal Retina, hPSC-Derived Retinal Organoids, and Long-Term Retinal Cultures. Cell Rep. *30*, 1644–1659.e4. https://doi.org/10.1016/J.CELREP.2020.01.007.

29. Schnitzer, J., and Rusoff, A.C. (1984). Horizontal cells of the mouse retina contain glutamic acid decarboxylase-like immunoreactivity during early developmental stages. J. Neurosci. *4*, 2948–2955. https://doi.org/10.1523/JNEUROSCI.04-12-02948.1984.

30. Demb, J.B., and Singer, J.H. (2015). Functional Circuitry of the Retina. Annu. Rev. Vis. Sci. *1*, 263–289. https://doi.org/10.1146/annurev-vision-082114-035334.

31. Amini, R., Bhatnagar, A., Schlüßler, R., Möllmert, S., Guck, J., and Norden, C. (2022). Amoeboid-like migration ensures correct horizontal cell layer formation in the developing vertebrate retina. eLife *11*, 1–30. https://doi.org/10.7554/elife.76408.

32. Matejčić, M., Salbreux, G., and Norden, C. (2018). A non-cell-autonomous actin redistribution enables isotropic retinal growth. PLoS Biol. *16*, e2006018. https://doi.org/10.1371/journal.pbio.2006018.

33. Ferme, L.C., Ryan, A.Q., Haase, R., Modes, C.D., and Norden, C. (2025). Timely neurogenesis drives the transition from nematic to crystalline nuclear packing during retinal morphogenesis. Sci. Adv. *11*, eadu6843. https://doi.org/10.1126/sciadv.adu6843.

34. Letelier, J., Buono, L., Almuedo-Castillo, M., Zang, J., Mounieres, C., González-Díaz, S., Polvillo, R., Sanabria-Reinoso, E., Corbacho, J., Sousa-Ortega, A., et al. (2023). Mutation of vsx genes in zebrafish highlights the robustness of the retinal specification network. eLife *12*, e85594. https://doi.org/10.7554/eLife.85594.

35. Passini, M.A., Levine, E.M., Canger, A.K., Raymond, P.A., and Schechter, N. (1997). Vsx-1 and vsx-2: Differential expression of two paired-like homeobox genes during zebrafish and goldfish retinogenesis. J. Comp. Neurol. *388*, 495–505.

36. Kroll, F., Powell, G.T., Ghosh, M., Gestri, G., Antinucci, P., Hearn, T.J., Tunbak, H., Lim, S., Dennis, H.W., Fernandez, J.M., et al. (2021). A simple and effective F0 knockout method for rapid screening of behaviour and other complex phenotypes. eLife *10*, e59683. https://doi.org/10.7554/eLife.59683.

37. Boije, H., Rulands, S., Dudczig, S., Simons, B.D., and Harris, W.A. (2015). The Independent Probabilistic Firing of Transcription Factors: A Paradigm for Clonal Variability in the Zebrafish Retina. Dev. Cell *34*, 532–543. https://doi.org/10.1016/j.devcel.2015.08.011.

38. Nerli, E., Kretzschmar, J., Bianucci, T., Rocha-Martins, M., Zechner, C., and Norden, C. (2023). Deterministic and probabilistic fate decisions co-exist in a single retinal lineage. EMBO J. *42*, e112657. https://doi.org/10.15252/embj.2022112657.

39. Randlett, O., MacDonald, R.B., Yoshimatsu, T., Almeida, A.D., Suzuki, S.C., Wong, R.O., and Harris, W.A. (2013). Cellular Requirements for Building a Retinal Neuropil. Cell Rep. *3*, 282–290. https://doi.org/10.1016/j.celrep.2013.01.020.

40. Chapot, C.A., Euler, T., and Schubert, T. (2017). How do horizontal cells 'talk' to cone photoreceptors? Different levels of complexity at the cone-horizontal cell synapse. J. Physiol. *595*, 5495–5506. https://doi.org/10.1113/JP274177.

41. Brzezinski, J.A., Uoon Park, K., and Reh, T.A. (2013). Blimp1 (Prdm1) prevents re-specification of photoreceptors into retinal bipolar cells by restricting competence. Dev. Biol. *384*, 194–204. https://doi.org/10.1016/J.YDBIO.2013.10.006.

42. Godinho, L., Mumm, J.S., Williams, P.R., Schroeter, E.H., Koerber, A., Park, S.W., Leach, S.D., and Wong, R.O.L. (2005). Targeting of amacrine cell neurites to appropriate synaptic laminae in the developing zebrafish retina. Development *132*, 5069–5079. https://doi.org/10.1242/dev.02075.

43. Jusuf, P.R., Almeida, A.D., Randlett, O., Joubin, K., Poggi, L., and Harris, W.A. (2011). Origin and Determination of Inhibitory Cell Lineages in the Vertebrate Retina. J. Neurosci. *31*, 2549–2562. https://doi.org/10.1523/JNEUROSCI.4713-10.2011.

44. Nakhai, H., Sel, S., Favor, J., Mendoza-Torres, L., Paulsen, F., Duncker, G.I.W., and Schmid, R.M. (2007). Ptf1a is essential for the differentiation of GABAergic and glycinergic amacrine cells and horizontal cells in the mouse retina. Development *134*, 1151–1160. https://doi.org/10.1242/dev.02781.

45. Boije, H., Edqvist, P.-H.D., and Hallböök, F. (2008). Temporal and spatial expression of transcription factors FoxN4, Ptf1a, Prox1, Isl1 and Lim1 mRNA in the developing chick retina. Gene Expr. Patterns *8*, 117–123. https://doi.org/10.1016/j.modgep.2007.09.004.

46. Wu, F., Li, R., Umino, Y., Kaczynski, T.J., Sapkota, D., Li, S., Xiang, M., Fliesler, S.J., Sherry, D.M., Gannon, M., et al. (2013). Onecut1 is essential for horizontal cell genesis and retinal integrity. J. Neurosci. *33*, 13053–13065. https://doi.org/10.1523/JNEUROSCI.0116-13.2013.

47. Klimova, L., Antosova, B., Kuzelova, A., Strnad, H., and Kozmik, Z. (2015). Onecut1 and Onecut2 transcription factors operate downstream of Pax6 to regulate horizontal cell development. Dev. Biol. *402*, 48–60. https://doi.org/10.1016/J.YDBIO.2015.02.023.

48. Schick, E., Gonzalez, K.C., Dutta, P., Hossain, K., Ghinia Tegla, M.G., and Emerson, M.M. (2021). Early cis-regulatory events in the formation of retinal horizontal cells. Dev. Biol. *476*, 88–100. https://doi.org/10.1016/j.ydbio.2021.03.016.

49. Wiseglass, G., Boni, N., Smorodinsky-Atias, K., and Rubinstein, R. (2024). Clustered protocadherin cis-interactions are required for combinatorial cell–cell recognition underlying neuronal self-avoidance. Proc. Natl. Acad. Sci. *121*, e2319829121. https://doi.org/10.1073/pnas.2319829121.

50. Lv, X., Li, S., Li, J., Yu, X.Y., Ge, X., Li, B., Hu, S., Lin, Y., Zhang, S., Yang, J., et al. (2022). Patterned cPCDH expression regulates the fine organization of the neocortex. Nature *612*, 503–511. https://doi.org/10.1038/s41586-022-05495-2.

51. Hou, R., Denisenko, E., Ong, H.T., Ramilowski, J.A., and Forrest, A.R.R. (2020). Predicting cell-to-cell communication networks using NATMI. Nat. Commun. *11*, 5011. https://doi.org/10.1038/s41467-020-18873-z.

52. López-Bendito, G., Flames, N., Ma, L., Fouquet, C., Di Meglio, T., Chedotal, A., Tessier-Lavigne, M., and Marín, O. (2007). Robo1 and Robo2 Cooperate to Control the Guidance of Major Axonal Tracts in the Mammalian Forebrain. J. Neurosci. *27*, 3395–3407. https://doi.org/10.1523/JNEUROSCI.4605-06.2007.

53. Hammond, R., Vivancos, V., Naeem, A., Chilton, J., Mambetisaeva, E., Andrews, W., Sundaresan, V., and Guthrie, S. (2005). Slit-mediated repulsion is a key regulator of motor axon pathfinding in the hindbrain. Development *132*, 4483–4495. https://doi.org/10.1242/dev.02038.

54. Blockus, H., and Chédotal, A. (2016). Slit-Robo signaling. Development *143*, 3037–3044. https://doi.org/10.1242/DEV.132829.

55. Nóbrega-Pereira, S., Kessaris, N., Du, T., Kimura, S., Anderson, S.A., and Marín, O. (2008). Postmitotic Nkx2-1 Controls the Migration of Telencephalic Interneurons by Direct Repression of Guidance Receptors. Neuron *59*, 733–745. https://doi.org/10.1016/j.neuron.2008.07.024.

56. Marín, O., Yaron, A., Bagri, A., Tessier-Lavigne, M., and Rubenstein, J.L.R. (2001). Sorting of Striatal and Cortical Interneurons Regulated by Semaphorin-Neuropilin Interactions. Science *293*, 872–875. https://doi.org/10.1126/science.1061891.

57. Baloh, R.H., Enomoto, H., Johnson, E.M., and Milbrandt, J. (2000). The GDNF family ligands and receptors — implications for neural

development. Curr. Opin. Neurobiol. *10*, 103–110. https://doi.org/10.1016/S0959-4388(99)00048-3.

58. Lamballe, F., Klein, R., and Barbacid, M. (1991). *trk*C, a new member of the *trk* family of tyrosine protein kinases, is a receptor for neurotrophin-3. Cell *66*, 967–979. https://doi.org/10.1016/0092-8674(91)90442-2.
59. Kotzbauer, P.T., Lampe, P.A., Heuckeroth, R.O., Golden, J.P., Creedon, D.J., Johnson, E.M., Jr., and Milbrandt, J. (1996). Neurturin, a relative of glial-cell-line-derived neurotrophic factor. Nature *384*, 467–470. https://doi.org/10.1038/384467a0.
60. Young, H.M., Anderson, R.B., and Anderson, C.R. (2004). Guidance cues involved in the development of the peripheral autonomic nervous system. Auton. Neurosci. *112*, 1–14. https://doi.org/10.1016/j.autneu.2004.02.008.
61. Chu, Y., and Kordower, J.H. (2023). Post-Mortem Studies of Neurturin Gene Therapy for Parkinson's Disease: Two Subjects with 10 Years CERE120 Delivery. Mov. Disord. *38*, 1728–1736. https://doi.org/10.1002/mds.29518.
62. Zanin, J.P., Battiato, N.L., and Rovasio, R.A. (2013). Neurotrophic factor NT-3 displays a non-canonical cell guidance signaling function for cephalic neural crest cells. Eur. J. Cell Biol. *92*, 264–279. https://doi.org/10.1016/j.ejcb.2013.10.006.
63. Chalazonitis, A. (2004). Neurotrophin-3 in the development of the enteric nervous system. In Progress in Brain Research NGF and Related Molecules in Health and Disease (Elsevier), pp. 243–263. https://doi.org/10.1016/S0079-6123(03)46016-0.
64. Kidd, T., Brose, K., Mitchell, K.J., Fetter, R.D., Tessier-Lavigne, M., Goodman, C.S., and Tear, G. (1998). Roundabout Controls Axon Crossing of the CNS Midline and Defines a Novel Subfamily of Evolutionarily Conserved Guidance Receptors. Cell *92*, 205–215. https://doi.org/10.1016/S0092-8674(00)80915-0.
65. Kidd, T., Bland, K.S., and Goodman, C.S. (1999). Slit Is the Midline Repellent for the Robo Receptor in Drosophila. Cell *96*, 785–794. https://doi.org/10.1016/S0092-8674(00)80589-9.
66. Jaworski, A., Long, H., and Tessier-Lavigne, M. (2010). Collaborative and specialized functions of Robo1 and Robo2 in spinal commissural axon guidance. J. Neurosci. *30*, 9445–9453. https://doi.org/10.1523/JNEUROSCI.6290-09.2010.
67. Fricke, C., Lee, J.S., Geiger-Rudolph, S., Bonhoeffer, F., and Chien, C.B. (2001). astray, a Zebrafish roundabout homolog required for retinal axon guidance. Science *292*, 507–510. https://doi.org/10.1126/science.1059496.
68. Campbell, D.S., Stringham, S.A., Timm, A., Xiao, T., Law, M.Y., Baier, H., Nonet, M.L., and Chien, C.B. (2007). Slit1a Inhibits Retinal Ganglion Cell Arborization and Synaptogenesis via Robo2-Dependent and -Independent Pathways. Neuron *55*, 231–245. https://doi.org/10.1016/J.NEURON.2007.06.034.
69. Davison, C., and Zolessi, F.R. (2021). Slit2 is necessary for optic axon organization in the zebrafish ventral midline. Cells Dev. *166*, 203677. https://doi.org/10.1016/J.CDEV.2021.203677.
70. Jia, L., Cheng, L., and Raper, J. (2005). Slit/Robo signaling is necessary to confine early neural crest cells to the ventral migratory pathway in the trunk. Dev. Biol. *282*, 411–421. https://doi.org/10.1016/j.ydbio.2005.03.021.
71. Wu, J.Y., Feng, L., Park, H.-T., Havlioglu, N., Wen, L., Tang, H., Bacon, K.B., Jiang, Z., Zhang, X., and Rao, Y. (2001). The neuronal repellent Slit inhibits leukocyte chemotaxis induced by chemotactic factors. Nature *410*, 948–952. https://doi.org/10.1038/35073616.
72. Lee, J.-S., Ray, R., and Chien, C.-B. (2001). Cloning and expression of three zebrafish roundabout homologs suggest roles in axon guidance and cell migration. Dev. Dyn. *221*, 216–230. https://doi.org/10.1002/dvdy.1136.
73. Samuel, A., Rubinstein, A.M., Azar, T.T., Ben-Moshe Livne, Z., Kim, S.-H., and Inbal, A. (2016). Six3 regulates optic nerve development via multiple mechanisms. Sci. Rep. *6*, 20267. https://doi.org/10.1038/srep20267.
74. Moore, R.E., Clarke, J., and Alexandre, P. (2020). Protrusion-Mediated Signaling Regulates Patterning of the Developing Nervous System. Front. Cell Dev. Biol. *8*, 579073. https://doi.org/10.3389/fcell.2020.579073.
75. Jacquemet, G., Hamidi, H., and Ivaska, J. (2015). Filopodia in cell adhesion, 3D migration and cancer cell invasion. Curr. Opin. Cell Biol. *36*, 23–31. https://doi.org/10.1016/J.CEB.2015.06.007.
76. McConnell, R.E., Edward van Veen, J., Vidaki, M., Kwiatkowski, A.V., Meyer, A.S., and Gertler, F.B. (2016). A requirement for filopodia extension toward Slit during Robo-mediated axon repulsion. J. Cell Biol. *213*, 261–274. https://doi.org/10.1083/jcb.201509062.
77. Huckfeldt, R.M., Schubert, T., Morgan, J.L., Godinho, L., Di Cristo, G., Huang, Z.J., and Wong, R.O.L. (2009). Transient neurites of retinal horizontal cells exhibit columnar tiling via homotypic interactions. Nat. Neurosci. *12*, 35–43. https://doi.org/10.1038/nn.2236.
78. Zhang, C., Gao, J., Zhang, H., Sun, L., and Peng, G. (2012). Robo2–Slit and Dcc–Netrin1 Coordinate Neuron Axonal Pathfinding within the Embryonic Axon Tracts. J. Neurosci. *32*, 12589–12602. https://doi.org/10.1523/JNEUROSCI.6518-11.2012.
79. Gambarotto, D., Zwettler, F.U., Le Guennec, M., Schmidt-Cernohorska, M., Fortun, D., Borgers, S., Heine, J., Schloetel, J.-G., Reuss, M., Unser, M., et al. (2019). Imaging cellular ultrastructures using expansion microscopy (U-ExM). Nat. Methods *16*, 71–74. https://doi.org/10.1038/s41592-018-0238-1.
80. Steib, E., Vagena-Pantoula, C., and Vermot, J. (2023). TissUExM protocol for ultrastructure expansion microscopy of zebrafish larvae and mouse embryos. STAR Protoc. *4*, 102257. https://doi.org/10.1016/J.XPRO.2023.102257.
81. Sariola, H., and Saarma, M. (2003). Novel functions and signalling pathways for GDNF. J. Cell Sci. *116*, 3855–3862. https://doi.org/10.1242/jcs.00786.
82. Cooper, J.A. (2014). Molecules and mechanisms that regulate multipolar migration in the intermediate zone. Front. Cell. Neurosci. *8*, 386. https://doi.org/10.3389/fncel.2014.00386.
83. Heller, E., and Fuchs, E. (2015). Tissue patterning and cellular mechanics. J. Cell Biol. *211*, 219–231. https://doi.org/10.1083/jcb.201506106.
84. Ypsilanti, A.R., Zagar, Y., and Chédotal, A. (2010). Moving away from the midline: new developments for Slit and Robo. Development *137*, 1939–1952. https://doi.org/10.1242/dev.044511.
85. Cacalano, G., Fariñas, I., Wang, L.-C., Hagler, K., Forgie, A., Moore, M., Armanini, M., Phillips, H., Ryan, A.M., Reichardt, L.F., et al. (1998). GFRα1 Is an Essential Receptor Component for GDNF in the Developing Nervous System and Kidney. Neuron *21*, 53–62. https://doi.org/10.1016/S0896-6273(00)80514-0.
86. Garcès, A., Haase, G., Airaksinen, M.S., Livet, J., Filippi, P., and deLapeyrière, O. (2000). GFRα1 Is Required for Development of Distinct Subpopulations of Motoneuron. J. Neurosci. *20*, 4992–5000. https://doi.org/10.1523/JNEUROSCI.20-13-04992.2000.
87. Brantley, M.A., Jain, S., Barr, E.E., Johnson, E.M., and Milbrandt, J. (2008). Neurturin-Mediated Ret Activation Is Required for Retinal Function. J. Neurosci. *28*, 4123–4135. https://doi.org/10.1523/JNEUROSCI.0249-08.2008.
88. Karlsson, M., Lindqvist, N., Mayordomo, R., and Hallböök, F. (2002). Overlapping and specific patterns of GDNF, c-ret and GFRα mRNA expression in the developing chicken retina. Mech. Dev. *114*, 161–165. https://doi.org/10.1016/S0925-4773(02)00045-X.
89. Almeida, A.D., Boije, H., Chow, R.W., He, J., Tham, J., Suzuki, S.C., and Harris, W.A. (2014). Spectrum of Fates: A new approach to the study of the developing zebrafish retina. Dev. Camb. *141*, 1971–1980. https://doi.org/10.1242/dev.104760.

90. Zolessi, F.R., Poggi, L., Wilkinson, C.J., Chien, C.-B., and Harris, W.A. (2006). Polarization and orientation of retinal ganglion cells in vivo. Neural Dev. *1*, 2. https://doi.org/10.1186/1749-8104-1-2.

91. Swanhart, L.M., Takahashi, N., Jackson, R.L., Gibson, G.A., Watkins, S.C., Dawid, I.B., and Hukriede, N.A. (2010). Characterization of an lhx1a transgenic reporter in zebrafish. Int. J. Dev. Biol. *54*, 731–736. https://doi.org/10.1387/ijdb.092969ls.

92. Parsons, M.J., Pisharath, H., Yusuff, S., Moore, J.C., Siekmann, A.F., Lawson, N., and Leach, S.D. (2009). Notch-responsive cells initiate the secondary transition in larval zebrafish pancreas. Mech. Dev. *126*, 898–912. https://doi.org/10.1016/j.mod.2009.07.002.

93. Schroeter, E.H., Wong, R.O.L., and Gregg, R.G. (2006). In vivo development of retinal ON-bipolar cell axonal terminals visualized in nyx::MYFP transgenic zebrafish. Vis. Neurosci. *23*, 833–843. https://doi.org/10.1017/S0952523806230219.

94. Jusuf, P.R., Albadri, S., Paolini, A., Currie, P.D., Argenton, F., Higashijima, S.i., Harris, W.A., and Poggi, L. (2012). Biasing Amacrine Subtypes in the Atoh7 Lineage through Expression of Barhl2. J. Neurosci. *32*, 13929–13944. https://doi.org/10.1523/JNEUROSCI.2073-12.2012.

95. Geldmacher-Voss, B., Reugels, A.M., Pauls, S., and Campos-Ortega, J.A. (2003). A 90° rotation of the mitotic spindle changes the orientation of mitoses of zebrafish neuroepithelial cells. Development *130*, 3767–3780. https://doi.org/10.1242/dev.00603.

96. Kimura, Y., Satou, C., and Higashijima, S.I. (2008). V2a and V2b neurons are generated by the final divisions of pair-producing progenitors in the zebrafish spinal cord. Development *135*, 3001–3005. https://doi.org/10.1242/dev.024802.

97. Anbalagan, S., Blechman, J., Gliksberg, M., Gordon, L., Rotkopf, R., Dadosh, T., Shimoni, E., and Levkowitz, G. (2019). Robo2 regulates synaptic oxytocin content by affecting actin dynamics. eLife *8*, e45650. https://doi.org/10.7554/eLife.45650.

98. Panza, P., Maier, J., Schmees, C., Rothbauer, U., and Söllner, C. (2015). Live imaging of endogenous protein dynamics in zebrafish using chromobodies. Dev. Camb. *142*, 1879–1884. https://doi.org/10.1242/dev.118943.

99. Liao, Y., Smyth, G.K., and Shi, W. (2014). featureCounts: an efficient general purpose program for assigning sequence reads to genomic features. Bioinforma. Oxf. Engl. *30*, 923–930. https://doi.org/10.1093/bioinformatics/btt656.

100. Love, M.I., Huber, W., and Anders, S. (2014). Moderated estimation of fold change and dispersion for RNA-seq data with DESeq2. Genome Biol. *15*, 550. https://doi.org/10.1186/s13059-014-0550-8.

101. Wickham, H. (2016). ggplot2 (Springer). https://doi.org/10.1007/978-3-319-24277-4.

102. Slowikowski, K. (2024). ggrepel: Automatically Position Non-Overlapping Text Labels with "ggplot2" https://github.com/slowkow/ggrepel.

103. Dobin, A., Davis, C.A., Schlesinger, F., Drenkow, J., Zaleski, C., Jha, S., Batut, P., Chaisson, M., and Gingeras, T.R. (2013). STAR: ultrafast universal RNA-seq aligner. Bioinformatics *29*, 15–21. https://doi.org/10.1093/bioinformatics/bts635.

104. Kolde, R. (2010). Pheatmap: pretty heatmaps. R package version. https://doi.org/10.32614/CRAN.package.pheatmap.

105. Schindelin, J., Arganda-Carreras, I., Frise, E., Kaynig, V., Longair, M., Pietzsch, T., Preibisch, S., Rueden, C., Saalfeld, S., Schmid, B., et al. (2012). Fiji: An open-source platform for biological-image analysis. Nat. Methods *9*, 676–682. https://doi.org/10.1038/nmeth.2019.

106. Daetwyler, S., Modes, C.D., and Fiolka, R. (2020). Fiji plugin for annotating movies with custom arrows. Biol. Open *9*, bio056200. https://doi.org/10.1242/bio.056200.

107. Stringer, C., and Pachitariu, M. (2025). Cellpose3: one-click image restoration for improved cellular segmentation. Nat. Methods *22*, 592–599. https://doi.org/10.1038/s41592-025-02595-5.

108. Kimmel, C.B., Ballard, W.W., Kimmel, S.R., Ullmann, B., and Schilling, T.F. (1995). Stages of Embryonic Development of the Zebrafish. Dev. Dyn. *203*, 253–310. https://doi.org/10.1002/aja.1002030302.

109. Leong, W.Y., Lim, Z.H., Korzh, V., Pietri, T., and Goh, E.L.K. (2015). Methyl-CpG Binding Protein 2 (Mecp2) Regulates Sensory Function Through Sema5b and Robo2. Front. Cell. Neurosci. *9*, 481. https://doi.org/10.3389/fncel.2015.00481.

110. Langheinrich, U., Hennen, E., Stott, G., and Vacun, G. (2002). Zebrafish as a Model Organism for the Identification and Characterization of Drugs and Genes Affecting p53 Signaling. Curr. Biol. *12*, 2023–2028. https://doi.org/10.1016/S0960-9822(02)01319-2.

111. Macaulay, I.C., Teng, M.J., Haerty, W., Kumar, P., Ponting, C.P., and Voet, T. (2016). Separation and parallel sequencing of the genomes and transcriptomes of single cells using G&T-seq. Nat. Protoc. *11*, 2081–2103. https://doi.org/10.1038/nprot.2016.138.

112. Baym, M., Kryazhimskiy, S., Lieberman, T.D., Chung, H., Desai, M.M., and Kishony, R. (2015). Inexpensive Multiplexed Library Preparation for Megabase-Sized Genomes. PLoS One *10*, e0128036. https://doi.org/10.1371/journal.pone.0128036.

113. Picelli, S., Faridani, O.R., Björklund, Å.K., Winberg, G., Sagasser, S., and Sandberg, R. (2014). Full-length RNA-seq from single cells using Smart-seq2. Nat. Protoc. *91*, 171–181. https://doi.org/10.1038/nprot.2014.006.

114. Labun, K., Montague, T.G., Krause, M., Torres Cleuren, Y.N., Tjeldnes, H., and Valen, E. (2019). CHOPCHOP v3: expanding the CRISPR web toolbox beyond genome editing. Nucleic Acids Res. *47*, W171–W174. https://doi.org/10.1093/nar/gkz365.

115. Moreno-Mateos, M.A., Vejnar, C.E., Beaudoin, J.-D., Fernandez, J.P., Mis, E.K., Khokha, M.K., and Giraldez, A.J. (2015). CRISPRscan: designing highly efficient sgRNAs for CRISPR-Cas9 targeting in vivo. Nat. Methods *12*, 982–988. https://doi.org/10.1038/nmeth.3543.

116. Butler, M.G., Iben, J.R., Marsden, K.C., Epstein, J.A., Granato, M., and Weinstein, B.M. (2015). SNPfisher: tools for probing genetic variation in laboratory-reared zebrafish. Dev. Camb. Engl. *142*, 1542–1552. https://doi.org/10.1242/dev.118786.

117. Robinson, J.T., Thorvaldsdóttir, H., Winckler, W., Guttman, M., Lander, E.S., Getz, G., and Mesirov, J.P. (2011). Integrative Genomics Viewer. Nat. Biotechnol. *29*, 24–26. https://doi.org/10.1038/nbt.1754.

118. Damstra, H.G.J., Mohar, B., Eddison, M., Akhmanova, A., Kapitein, L.C., and Tillberg, P.W. (2022). Visualizing cellular and tissue ultrastructure using Ten-fold Robust Expansion Microscopy (TREx). eLife *11*, e73775. https://doi.org/10.7554/eLife.73775.

119. Sim, J., Park, C.E., Cho, I., Min, K., Eom, M., Han, S., Jeon, H., Cho, E.-S., Lee, Y., Yun, Y.H., et al. (2025). Nanoscale Resolution Imaging of Whole Mouse Embryos Using Expansion Microscopy. ACS Nano *19*, 7910–7927. https://doi.org/10.1021/acsnano.4c14791.

120. Korovesi, A.G., Morgado, L., Fumasoni, M., Henriques, R., Heil, H.S., and Del Rosario, M. (2022). Expansion Microscopy on Saccharomyces cerevisiae. MicroPubl. Biol. *2022*, 10. https://doi.org/10.17912/MICROPUB.BIOLOGY.000566.

121. Thisse, C., and Thisse, B. (2008). High-resolution in situ hybridization to whole-mount zebrafish embryos. Nat. Protoc. *3*, 59–69. https://doi.org/10.1038/nprot.2007.514.

122. Sinigaglia, C. (2019). A Widely Applicable Urea-based Fluorescent/Colorimetric mRNA in situ Hybridization Protocol. Bio. Protoc. *9*, e3360. https://doi.org/10.21769/bioprotoc.3360.

STAR★METHODS

KEY RESOURCES TABLE

REAGENT or RESOURCE	SOURCE	IDENTIFIER
Antibodies		
GFP tag	Proteintech	Cat# 50430-2-AP; RRID: AB_11042881
HuC/HuD (16A11)	Molecular Probes	Cat# A-21271; RRID: AB_221448
Zpr-1	Zebrafish International Resource Center	Cat# zpr-1; RRID: AB_10013803
Prox1	Millipore	Cat# AB5475; RRID: AB_177485
Robo2 (E4M6D)	Cell Signaling Technology	Cat# 45568; RRID: AB_2799284
Alexa Fluor 488 anti-rabbit	Thermo Fisher Scientific	Cat# A-11034; RRID: AB_2576217
Alexa Fluor 647 anti-rabbit	Thermo Fisher Scientific	Cat# A-21245; RRID: AB_2535813
Alexa Fluor 647 anti-mouse	Thermo Fisher Scientific	Cat# A-21236; RRID: AB_2535805
Critical commercial assays		
DIG RNA Labeling Kit (SP6/T7)	Roche	Cat# 11175025910
Deposited data		
RNA-seq of Danio rerio photoreceptors, amacrine- and horizontal cells, collected 38-,48- and 58 hours post fertilization	This paper	https://www.ebi.ac.uk/ena/browser/view/PRJEB80557
Manually curated Human and Zebrafish Orthology	Zebrafish Information Network (ZFIN)	https://zfin.org/downloads/human_orthos.txt
Zebrafish reference genome GRCz11	Genome Reference Consortium	https://www.ncbi.nlm.nih.gov/datasets/genome/GCF_000002035.6/
Experimental models: Organisms/strains		
Zebrafish: wild-type AB	EZRC	EZRC: 1175
Zebrafish: wild-type TL	EZRC	EZRC: 1174
Zebrafish: Tg(crx:gap-CFP), Tg(ptf1a:Gal4/UAS:gap-YFP) and Tg(atoh7:gap-RFP)	Almeida et al.[89]	ZDB-FISH-150901-28125
Zebrafish: Tg(atoh7:gap-RFP)	Zolessi et al.[90]	ZDB-GENO-070130-1
Zebrafish: Tg(lhx1:GFP)	Swanhart et al.[91]	ZDB-GENO-100625-1
Zebrafish: Tg(ptf1a:Gal4/UAS:gap-YFP)	Parsons et al.[92] Schroeter et al.[93]	ZDB-GENO-110915-2
Zebrafish: Tg(ptf1a:dsRed)	Jusuf et al.[94]	ZDB-GENO-101201-2
Zebrafish: Tg(h2az2a:h2az2a-GFP)	Geldmacher-Voss et al.[95]	ZDB-GENO-020717-1
Zebrafish: Tg(vsx1:GFP)	Kimura et al.[96]	ZDB-GENO-090116-2
Zebrafish: Robo2$^{-/-}$; Tg(lhx1:GFP); Tg(ptf1a:dsRed)	This paper	N/A
Oligonucleotides		
Morpholino: MO1-ptf1a CCAACACAGTGTCCATTTTTTGTGC	Gene Tools	ZDB-MRPHLNO-070531-6
Morpholino: MO4-ptf1a TTGCCCAGTAACAACAATCGCCTAC	Gene Tools	ZDB-MRPHLNO-070531-9
Morpholino: MO6-robo2 GTAGCGCAACTCACCATCACTTGG	Gene Tools	ZDB-MRPHLNO-121016-4
Morpholino: MO-Neurturin TGGCAGCAAACTTCCATAACTTCAT	Gene Tools	N/A
Morpholino: MO-Neurturin-like CATACCCTCATCTTAGAGCAGCGTG	Gene Tools	N/A
Morpholino: MO4-tp53 GCGCCATTGCTTTGCAAGAATTG	Gene Tools	ZDB-MRPHLNO-070126-7

(*Continued on next page*)

Continued

REAGENT or RESOURCE	SOURCE	IDENTIFIER
Primer: Slit2-T7 TAATACGACTCACTATAGGCAACA GAGAATCCTTCCTGC	This paper	N/A
Primer: Slit2-SP6 ATTTAGGTGACACTATAGATGCGT CTGATAGTGATCTCG	This paper	N/A
Primer: Robo2-T7 TAATACGACTCACTATAGGTGTA CAGGCAGATGTCAGGC	Anbalagan et al.[97]	N/A
Primer: Robo2-SP6 ATTTAGGTGACACTATAGATCCT CCTCCAGTAGAGCCAG	Anbalagan et al.[97]	N/A
Recombinant DNA		
Tol2-UAS:Robo2-mCherry	This paper	N/A
pDEST-ptf1a:Gal4	N/A	N/A
UAS:ActinCB-TagGFP2	Panza et al.[98]	N/A
Software and algorithms		
R (v4.4.1)	R Core Team, 2024	https://cran.r-project.org/index.html
featureCounts	Liao et al.[99]	https://subread.sourceforge.net/featureCounts.html
DESeq2 (v1.44)	Love et al.[100]	https://bioconductor.org/packages/release/bioc/html/DESeq2.html
ggplot2 (v3.5.1)	Wickham,[101]	https://ggplot2.tidyverse.org/
Ggrepel (v0.9.6)	Slowikowski,[102]	https://ggrepel.slowkow.com/
STAR (v2.7.0)	Dobin et al.[103]	https://github.com/alexdobin/STAR
Network Analysis Toolkit for Multicellular Interactions (NATMI)	Hou et al.[51]	https://github.com/forrest-lab/NATMI
pheatmap (v1.0.12)	Kolde,[104]	https://CRAN.R-project.org/package=pheatmap
ZEN Microscopy software (v3.3, blue edition)	Zeiss	https://www.zeiss.com/microscopy/en/products/software/zeiss-zen.html
Fiji	Schindelin et al.[105]	https://imagej.net/software/fiji/#publication
DrawArrowInMovie Plugin for Fiji	Daetwyler et al.[106]	https://github.com/DaetwylerStephan/draw_arrow_in_movies
Imaris (v10.0.0)	Oxford Instruments	https://imaris.oxinst.com/
OpenShot Video Editor	OpenShot Studios, LLC	https://www.openshot.org/
Inkscape (v1.2.3)	The Inkscape Project	https://inkscape.org/
bioicons	N/A	https://bioicons.com/
Prism (v9.4.0)	GraphPad Software	https://www.graphpad.com/
Cellpose (v3.0.8)	Stringer et al.[107]	https://www.cellpose.org/

EXPERIMENTAL MODEL

Zebrafish husbandry

Wild-type (*Danio rerio*; AB and TL strains) and transgenic reporter lines were maintained and bred at 28°C (pH 7.0, conductivity 1000 μS/cm, 14-h light - 10-h dark cycle; Techniplast). Embryos for experiments were raised at 28.5°C or 32°C in E3 medium. Staging of embryos aged between 38 and 120 h postfertilization (hpf) was conducted according to Kimmel et al.[108] For embryos used in experimental setups, 0.2 mM 1-phenyl-2-thiourea (PTU) (10107703, Acros Organics) in E3 medium was applied to prevent pigmentation. For live-cell imaging and retina dissection, embryos were anesthetized with 0.04% tricaine methane sulfonate (MS-222) (1004671, Pharmaq) in E3 medium. All zebrafish-related work was conducted under the licensing from the DGAV (Directorate-General for Food and Veterinary, Portugal) and in accordance with the European Union directive 2010/63/EU and with the Portuguese Decree Law n° 113/2013.

Zebrafish transgenic lines

A triple transgenic line containing *Tg(crx:gap-CFP)*, *Tg(ptf1a:Gal4/UAS:gap-YFP)* and *Tg(atoh7:gap-RFP)*, transgenes was used to visualize all the retinal neurons.[89] *Tg(atoh7:gap-RFP)* was mated with *Tg(lhx1:GFP)*[91] to detect PRs and HCs, respectively. *Tg(ptf1a:Gal4/UAS:gap-YFP)* labeling retinal interneurons (ACs and HCs) were also used independently. To specifically visualize HCs and ACs, the two transgenes *Tg(lhx1:GFP)* and *Tg(ptf1a:dsRed)*[94] were used together or separately. *Tg(vsx1:GFP)*[96] was used together with the *Tg(ptf1a:dsRed)* to label the BCs and retinal interneurons (ACs and HCs), respectively.

METHOD DETAILS

DNA constructs and cloning

To construct the Tol2-UAS:Robo2-mCherry expression plasmid, Zebrafish Robo2 CDS, obtained from pCS2-Robo2[109] (a kind gift from E. Goh), was Gateway-cloned into pDONR221 to create pENTR(L1L2)-Robo2. This construct was then combined with pENTR(L4R1)-UAS, pENTR(R2L3)-mCherry and pDEST(R4R3)-Tol2pA2 (originally from Chi-Bin Chien Lab), in a multisite Gateway LR reaction to generate the Tol2-UAS:Robo2-mCherry. pDEST-ptf1a:Gal4 was a gift from J.Kaslin and UAS:ActinCB-TagGFP2[98] (ChromoTek), gifted by P.Panza.

DNA and morpholino injections of zebrafish embryos

For mosaic labeling of cells, purified plasmid DNA (Tol2-UAS:Robo2-mCherry or pDEST-ptf1a:Gal4 with UAS:ActinCB-TagGFP2) were diluted to 25 ng/μL in sterile dd$H_2$0 containing 0.05% phenol red (P3532, Merck), and 0.5–1 nanoL of the solution was injected to the cell of one-cell stage *Tg(ptf1a:Gal4; UAS:gap-YFP)* or wild-type embryos, respectively.

All morpholinos (MO) were obtained from Gene Tools, LLC, and injected into the yolk of the one-cell stage embryos. To deplete ACs & HCs, two ptf1a translation-blocking morpholinos, 5 ng each, (5′-CCAACACAGTGTCCATTTTTTGTGC-3′)[43] and (5′-TTGCCCAGTAACAACAATCGCCTAC-3′)[43] were injected together. Robo2 was targeted with 5ng of splice-blocking MO (5′-GTAGCGCAACTCACCATCACTTGG-3′).[78] For Neurturin depletion, 5 ng of Neurturin (5′-TGGCAGCAAACTTCCATAACTTCAT-3′) and 5 ng of Neurturin-like (5′-CATACCCTCATCTTAGAGCAGCGTG-3′), translation blocking MOs were jointly injected. All injections additionally contained 2ng of p53 MO (5′-GCGCCATTGCTTTGCAAGAATTG-3′)[110] to reduce potential apoptosis.

Whole-mount immunofluorescence staining of zebrafish embryos

All immunostainings were performed on embryos fixed with 4% paraformaldehyde (043368.9M, Thermo Fisher) in 1x PBS, either 3 h at room temperature (RT) or overnight at 4°C. After fixation, embryos were washed 4 × 15 min (min) with 0.5% Triton X- in PBS (PBS-T) followed by tissue permeabilization with 0.25% Trypsin-EDTA (10 min for 38 hpf, 15 min for 48–58 hpf, and 18 min for 72–120 hpf) on ice. Embryos were then rinsed 4x with PBS-T and blocked with 10% goat serum in PBS-T either overnight at 4°C or 3 h at RT.

Following primary antibodies, incubated for 72 h at 4°C, were used in the study 1:200 GFP (50430-2-AP, Proteintech), 1:800 HuC/D (A-21271 Invitrogen) 1:500 Zpr-1 (AB_10013803, Zirc), 1:800 Prox1 (AB5475, Sigma Aldrich), 1:50 Robo2 (45568, Cell Signaling, 90% epitope identity to zebrafish Robo2). All primary antibodies were diluted in 1% goat serum in PBS-T. Primary antibody incubation was followed by 5 × 30 min washes with PBS-T and 48-h incubation at 4°C with Alexa Fluor 488 goat anti-rabbit (A-11034, Invitrogen), Alexa Fluor 647 goat anti-rabbit (A-21245, Invitrogen) or Alexa Fluor 647 goat anti-mouse (A-21236, Invitrogen). Additionally, 2 μg/mL DAPI (MBD0015, Sigma Aldrich) or Alexa Fluor 647 Phalloidin (8940, Cell Signaling) was added to stain the nuclei and F-actin, respectively. Finally, embryos were washed 4 × 15 min with PBS-T, twice with PBS, and stored in PBS at 4°C protected from light, until imaging.

Retinae dissection and flow cytometry-based sorting of photoreceptor- amacrine- and horizontal cells

Tg(lhx1:GFP); Tg(ptf1a:dsRed) embryos, staged at 38, 48 and 58 hpf, were dechorionated, anesthetized with 0.04% MS-222 and then placed on a polymethylsiloxane (Sylgard 184, 761036, Merck) -coated dish with ice-cold PBS supplemented with 0.04% MS-222 and 4 mM EDTA (1084180100, Merck). The retinae were dissected and both lens and the retinal pigment epithelium were removed. Four biological replicates at each developmental stage were performed. 40–50 retinae were collected into a sterile Eppendorf. For each biological replicate, retinal cells were dissociated by removing the PBS-EDTA and incubating them for 10 min at 28°C, 350 rpm, with 1x TrypLE Express (12604013, Thermo Fisher), enhancing the dissociation by mechanical pipetting every 5 min during the incubation. The samples with dissociated retinal cells were then washed twice with ice-cold 1x RNase-free PBS (AM9625, Invitrogen) and filtered through a 100 μm nylon mesh for FACS sorting. PRs (GFP positive), ACs (DsRed-positive) and HCs (GFP and DsRed-double positive), were sorted according to their fluorescent reporter expression, with FACSAria IIu (100 μm nozzle, BD), collecting 300–500 cells of each cell type straight into respective tubes containing RLT Plus lysis buffer (1053393, Qiagen), snap frozen and stored at −80°C until RNA extraction. The same procedure was conducted for each three developmental stage and for each four biological replicates.

RNA sequencing and data processing

The polyA(+) mRNA was isolated from the snap-frozen PR, HC and AC samples using a oligo-dT capture, followed by reverse-transcription to cDNA and PCR-amplification as in.[111] The cDNA quality was confirmed with Fragment Analyzer (Advanced Analytical) and one biological replicate from 48 hpf PR samples was discarded due to low quality. The library preparation for next generation sequencing (NGS) was conducted by carrying out Nextera tagmentation (Illumina) as in.[112] The RNA-sequencing was carried out according to Smart-seq2[113] using both NextSeq500 and NextSeg2000 systems (Illumina). The sequencing data is accessible at European Nucleotide Archive under project PRJEB80557. The RNA-seq datasets were aligned to the zebrafish reference genome GRCz11 with STAR (v2.7.0). Gene expression levels were quantified with Subread featureCounts.[99] For downstream analysis, the count matrix was normalized and transformed using the DESeq2[100] (v1.44) in R (v4.4.1). Differential expression (DE) significance was evaluated by p-value <0.05 and a log2 fold change >1, with variance-stabilizing transformation (VST). Visualization of the DE genes was performed using the ggplot2 (v3.5.1) and ggrepel (v0.9.6).

NATMI analysis

Network Analysis Toolkit for Multicellular Interactions (NATMI)[51] was downloaded from the Github (github.com/forrest-lab/NATMI/) repository. Next, zebrafish connectomeDB (Table S1) was constructed together with the authors of the original NATMI paper.[51] Shortly, zebrafish ortholog genes were obtained by manual merging of the NCBI homologene database file with Zebrafish Information Network (ZFIN), Human and Zebrafish Orthology file (human_orthos_2022.05.15.txt). The merged zebrafish ortholog data was then cross correlated with human connectomeDB2020 (https://asrhou.github.io//NATMI/), removing zebrafish genes with no orthologs. The DESeg2-transformed transcriptomic data were preprocessed, and gene expression matrices and cell annotation files were generated following the NATMI GitHub repository. NATMI predicted directional, weighted cell communication networks based on the expression levels of ligands and their corresponding receptors in each cell type (PR, AC and HC) (Table S1). As a filtering and thresholding criteria, we first included only ligand-receptor interactions with both ligand and receptor average expression over the biological replicates exceeding 700 counts either at 48 hpf or at 58 hpf time point. After this, secondary filtering step was conducted, where ligand-receptor interactions with Log2 expression weight at 48hpf or at 58 hpf of $\geq$20 were included. To construct final heatmap visualizations, we lastly applied literature-based filtering, selecting only ligand-receptor pairs with indicated or suggested repulsive or attractive roles. The resulting communication networks were visualized using heatmaps created with the pheatmap(v1.0.12) package in R (v4.4.1).

Blastomere transplantation of Ptf1a depleted embryos

Recipient embryos (*Tg(lhx1:GFP)* or Robo2 F1 were injected at one-cell stage with ptf1a MOs or with crRNAs targeting asymmetrical exons of *nrtn+nrtn-like* respectively, as described above, over three biological replicates (transplantation of three donor clutches with three recipient clutches). Recipients, as well as donors *Tg(lhx1:GFP)*; *Tg(ptf1a:dsRed)* or *Tg(H2A.F/Z:GFP)*, were dechorionated at 256-cell stage on a glass dish using 2 mg/mL Pronase (P8811, Sigma-Aldrich), followed by 3x rinse with Danieau buffer (0.7 mM KCl, 58 mM, NaCl, 0.6 mM Ca(NO3)2, 0.4 mM MgSo4.7H2O and 5mM HEPES). Recipients were then transferred onto 1% agarose mold containing 6 $\times$ 25 wells to hold embryos. At midblastula stage, 10–100 cells from donor embryos were transplanted into the recipient embryos using a micromanipulator equipped with a 0.1 mm diameter glass needle and an Olympus SZX10 stereo microscope. Transplanted embryos were allowed to recover for 2 h at 32°C, prior moving them onto agarose-coated dishes with antibiotics (100 U of penicillin and streptomycin, Thermo Fisher) supplemented E3 at 28.5°C and growing them in E3 with 0.2 mM PTU until 48 hpf (for live-imaging) or 72 hpf (fixed analysis).

In vivo F0 CRISPR guide RNA design and screen

The guide RNA (gRNA) design for each targeted gene used in this study was based on[36] and associated protocol (dx.doi.org/10.17504/protocols.io.81wgb6r5qlpk/v1). Shortly, CHOPCHOP[114] was used to select three crRNAs targeting early asymmetrical exons when possible with highest (>80%) predicted frameshift mutation frequency[115] and potential off-targets having over three nucleotide mismatches. The selected crRNAs were further screened to exclude candidates with potential single nucleotide polymorphisms (SNPs).[116] The list of crRNAs used in this study are available in Table S1. All designed crRNAs (2 nmol each), Alt-R CRISPR-Cas9 tracrRNA (1072533), Alt-R S.p. Cas9 Nuclease V3 (1081058) and Duplex buffer (11-01-03-01) were ordered from IDT.

To perform the F0 CRISPR screen, the selected three crRNAs per target gene were complexed with tracrRNA and Cas9, respectively, pooled and injected into the yolk of early 1-cell stage *Tg(lhx1:GFP); Tg(ptf1a:dsRed)* embryos as in.[36] Injected embryos (>200) were grown to 72 hpf in the presence of 0.2 mM PTU in E3. Embryos were anesthetized with 0.04% MS-222 in E3 and placed into 96-well glass-bottom ZF plate (HDK-ZFA101, Funakoshi) enabling uniform larvae alignment. Each well was imaged with a Nikon Eclipse Ti widefield system, equipped with Andor Zyla 4.2 PLUS sCMOS camera and using Plan Apo Lambda D10$\times$ objective (Nikon), the TRITC and FITC filter sets and NIS Elements (v5.42) software platform. After imaging, embryos with abnormal (lhx1:GFP and ptf1a:dsRed positive) HC-cell layer were selected for further analysis. The selected embryos were fixed overnight at 4°C with 4% PFA and processed for whole-mount immunofluorescence staining as described above. Each F0 knockout image presented in the figures represents data from at least 20 analyzed embryos.

Robo2 F1 line generation and gDNA sequencing

The *Tg(lhx1:GFP); Tg(ptf1a:dsRed)* embryos were injected with three crRNAs targeting asymmetrical exons 5, 6 and 9 of *Robo2* as described above. Embryos were grown to 72 hpf and screened, selecting embryos with ectopically placed HCs in the AC layer. These embryos, without any additional visible defects, were grown to 3 months of age, after which caudal fin clipping was performed to ten F0 founders anesthetized with 0.02% MS-222. The clipped fins were incubated in a lysis buffer (50 mM Tris-HCl pH 8.5, 1 mM EDTA, 0.5% Tween 20, 200 μg/mL Proteinase K) for 2 h at 55°C and after for 10 min at 95°C, to isolate the gDNA.

CHOPCHOP[114]-suggested primers (Table S1) with overhang adapters (MiSeq system, Illumina), were then used to PCR amplify 200 bp area around each gRNA binding site from the gDNA of each F0 founder. After validating the correct amplicon size with agarose gel electrophoresis, the three amplicons were pooled together and sequenced with Illumina Miseq. The resulting sequencing data was aligned to the Zebrafish genome (GRCz11) and visualized with Integrative Genomics Viewer[117] (ver. 2.17.3). Four F0 fish (two males, two females) with frameshift mutations in exon 5 and/or exon 6, leading to early stop codon (Table S1) were grown and served as founders. All F1 embryos, grown from incross of the F0 founders, phenocopied the HCs ectopic location in the AC layer.

Expansion microscopy of the whole zebrafish larvae

Tg(lhx1:GFP) or *Tg(ptf1a:Gal4; UAS:gap-YFP)* embryos grown to 52- and 54 hpf in the presence of 0.2 mM PTU, were fixed overnight at 4°C with 4% PFA and expanded using an adapted UltraExM protocol based on.[79,118–120] Prior expansion, the *Tg(ptf1a:Gal4; UAS:gap-YFP)* embryos were stained with 1:200 GFP (50430-2-AP, Proteintech) whereas the *Tg(lhx1:GFP)* embryos were processed straight for expansion. The embryos were washed 3 × 15 min with PBS-T and incubated overnight at RT in linking solution (0.1 mg/mL acryloyl X-SE (Invitrogen, A20770) in 0.1% PBS-T). Monomer solution (38% w/v sodium acrylate (408220, Sigma Aldrich) 40% w/v acrylamide (A9099, Sigma Aldrich), 2% w/v N,N′-Methylenebisacrylamide (274135, Sigma Aldrich), all in ddH_2O) was applied to the samples, containing 1:40 546nm-Actin ExM (Chrometra) and 2 μg/mL DAPI (MBD0015, Sigma Aldrich) for F-actin and nuclei labeling. Embryos were incubated for 24 h in the dark, at RT.

For gelation, embryos were placed on pre-cooled gelation chambers onto which ice-cold monomer solution with 0.5% TEMED (1.10732, Sigma Aldrich) and 0.5% APS (9592.3, Roth) was added. Embryos were quickly aligned with the retina facing to the bottom of the gelation chamber and a coverslip was inverted on the top. Gelation proceeded for 10 min on ice, followed by incubation for 3 h at 37°C or 24 h at RT in the dark in a humidified chamber. Following gelation, A digestion buffer (50 mM Tris-HCl pH 8.0, 1 mM EDTA pH 8.0, 0.5% Triton X-100, 0.8 M Guanidine HCl) and 8 U/ml Proteinase K (New England Biolabs P8107S) in ddH_2O) were added and gels were incubated at RT for 16 h. After digestion, gels were transferred to ddH_2O to initiate expansion. The water was changed twice after 30 min, followed by overnight incubation at RT to allow for complete expansion. The expanded gels were cut to separate the expanded zebrafish heads, and these samples were immobilized with retina facing down onto 0.1 mg/mL poly-D-lysine (A3890401, Thermo Fisher) -coated glass coverslips. The samples were imaged in ddH_2O using an LSM 980 point-scanning confocal with Airyscan 2 Multiplex (Zeiss), operated in Airyscan SR mode through microcopy ZEN Blue v 3.3 (Zeiss) software and using LD-C Apochromat 40x/1.1 W Corr M27 water-immersion objective (Zeiss). Airyscan 3D-processing was then conducted with auto filters in ZEN Blue v3.3 (Zeiss).

In situ hybridization of whole mount embryos and retinal sections

Oligos to generate probes for detecting Slit2 mRNA as previously used in[69] were utilized, containing T7 promoter site for the Slit2 sense: 5′-TAATACGACTCACTATAGGCAACAGAGAATCCTTCCT GC-3′ and SP6 promoter site in the anti-sense 5′-ATTTAGGTGA CACTATAGATGCGTCTGATAG TGATCTCG -3′ were used to amplify 897 bp segment corresponding to Slit2 3′-region. Similarly Robo2 sense 5′-TAATACGACTCACTATAGGTGTACAGGCAGATGTCAGGC-3′ and anti-sense 5′-ATTTAGGTGACACTATAG ATCCTCCTCCAGTAGAGCCAG-3′ oligos documented in[97] and including additional T7 and SP6 sites, respectively, were used to amplify 642 bp segment corresponding to Robo2 3′-region. Using the PCR-amplified DNA as templates, the DIG-labeled mRNA probes were generated using the DIG RNA Labeling Kit (SP6/T7) (11175025910, Roche) and purified with Pure Link RNA Mini Kit (12183018A, Invitrogen). The dot blot assay using serial dilutions of each DIG-labeled probe, was conducted on a Hybond-N+ (Amersham) membrane and detected with 0.08 mg/mL nitro-blue tetrazolium (NBT) (11383213001,Roche) and 0.1 mg/mL 5-bromo-4-chloro-3′-indolyphosphate (BCIP) (11383221001, Roche) confirming the optimal labeling of each probe.

Zebrafish embryos at 38, 48 and 58 hpf, fixed overnight at 4°C with 4% PFA were dehydrated and kept in 100% methanol for 48 h. The embryos were gradually rehydrated, treated with 10 μg/mL Proteinase K (EO0491, Thermo Fisher) for 30 min at RT, and acetylated following the published protocols.[121,122] Each probe was added to the overnight pre-hybridized (65°C) embryos at 0.2 ng/μL in hybridization buffer and incubated for 24h at 65°C. Hybridization buffer was used as reported in,[122] except that it additionally included 50% de-ionized formamide (F9037, Sigma Aldrich). The wash buffers I-III further contained 25%, 12,5% and 0% of the de-ionized formamide, respectively. Following the hybridization, embryos were washed, blocked and the colorimetric signal detection was performed as in.[122] In brief, for colorimetric signal detection 1:2000 dilution of anti-DIG-AP (11093274910, Roche) was applied overnight at 4°C, followed by washes and color development with 0.08 mg/mL NBT, 0.1 mg/mL BCIP in RT, protected from light. Part of the embryos of each developmental stage that were probed for both Slit2 and Robo2, were embedded overnight at 4°C in 30% sucrose-PBS, transferred to O.C.T (4583, Sakura) and cryosectioned with Cryostat 3050S (Leica) to 20 μm sections. Both, the whole-mount and sectioned hybridized embryos were imaged using a Zeiss Stereo Lumar.V12 stereo microscope, equipped with UI-3370CP Rev. 2 (Imaging Development Systems, IDS) color camera operated with uEye (IDS).

Spinning disk live-imaging of zebrafish embryos

To perform live-imaging of HC migration in controls or upon perturbations (MOs or KOs), between 5 and 20 embryos, anesthetized with 0.04% MS-222, were embedded into 0.7% low-melting agarose (A9045, Sigma Aldrich) in E3 medium. Either glass-bottom 35mm dishes (P35G-1.5-14-C, MatTek) or 2-well glass-bottom μ-slides (80286, Ibidi) were used for embedding. 15 min post embedding, when the agarose was solidified, the dish was filled with 32°C E3 medium containing 0.2 mM PTU and 0.04% MS-222. Imaging was conducted at 32°C using Marianas SDC (Intelligent Imaging Innovations, 3I) spinning disk confocal, operated through Nikon Ti2 Eclipse and Slidebook 2024 (3I) software platform and equipped with Yokogawa CSU-W1 scanner plus the Uniformizer (Yokogawa), and Photometrics Prime 95B sCMOS (Teledyne) camera. The imaging dish was allowed to settle to 32°C for 30 min prior the onset of acquisition. Z-stacks of 80 μm with 1 μm step size, were acquired every 10–20 min using 40x CFI Plan Apo Lambda S 40× Sil objective (Nikon). Embryos were imaged for a total of 12–24 h, depending on the experimental set up.

Airyscan confocal scan of whole-mount zebrafish retinae

Whole-mount, stained embryos between 38 and 120 hpf, were embedded into 1% low-melting agarose (A9045, Sigma Aldrich) in E3 medium and their retinae were imaged using an LSM 980 point-scanning confocal with Airyscan 2 Multiplex (Zeiss), using the Airyscan 2 detector and LD-C Apochromat 40x/1.1 W Corr M27 water-immersion objective (Zeiss). Acquisition was conducted in SR-8Y multiplex mode, operated through microcopy ZEN Blue v3.3 (Zeiss) software. 50 μm Z-stacks with 1 μm step size were acquired that were subsequently Airyscan 3D-processed using the auto filters in ZEN Blue v3.3 (Zeiss).

Image processing and analysis

Imaging data was processed using Fiji.[105] Data from live-imaging experiments was processed with 3D median filter (x,y,z; 2.0), cropped and Z-projected (Maximum intensity projection). Visualization of cell tracks for the videos were performed with DrawArrowInMovie-tool.[106] Imaris (v10.0.0, Oxford Instruments) was used for 3D-rendering the Z-projections of expanded retinae imaging data. Openshot Video editor (OpenShot Studios, LLC) was employed to concatenate the videos and add titles. Inkscape (v1.2.3) was used for the figure generation and bioicons (bioicons.com) for drawing illustrations.

QUANTIFICATION AND STATISTICAL ANALYSIS

Quantitative analysis of HCs in the AC-layer in different F0 knockouts

To count HCs in the AC-layer upon introduction of different KOs, HCs were segmented from 72- or 80 hpf fixed whole-mount *Tg(lhx1:GFP)* [HCs, PRs]; *Tg(ptf1a:dsRed)* [HCs, ACs] DAPI-stained KO retinae (20 μm maximum intensity Z-projections), using the GFP signal for cyto3 segmentation network in Cellpose v3.0.8.[107] The resulting outline ROIs from segmented cells were then transferred to Fiji with the respective maximum intensity projection and there a 130 × 300 μm area (excluding ciliary marginal zone) from each sample, was analyzed for HC positioning. Prior counting the cells, the ptf1a:dsRed signal was utilized to manually remove any DsRed-negative ROIs (PRs). All the cell ROIs within the 130 × 300 μm area were counted and binned either as laminated (if ≤ 5 μm from PR cell layer) or as stuck (>5 μm from the PR cell layer). Nuclei staining (DAPI) was used to determine the PR cell layer as well as the general retina lamination. Finally, the ratio of stuck to total HCs counted was used in the quantitative analysis (Table S1).

Analysis of HC cytokinesis positions

Divisions occurring in *Tg(lhx1:GFP); Tg(ptf1a:dsRed)* embryos injected RNPs targeting either *Scrambled* or *Robo2* and imaged from 48 hpf to 72 hpf, the HC (lhx1:GFP and ptf1a:dsRed positive) were manually located from a set ROI registering the same area in the nasal-temporal retinal axis. The position of mitotic HCs, respective to the basal side of the PRs (lhx1:GFP positive), were manually measured using the Fiji Line tool as in[24] (Table S1). To track the sister HC final positioning, both sister cells from each division event were manually tracked until the end of lamination (72 hpf) and cross-correlated with the division position.

Statistical analysis and reproducibility

All statistical tests were conducted using the GraphPad Prism v9.4.0. All analyzed data was first tested for normality, using Anderson-Darling and Shapiro-Wilk tests. As the analyzed data was not normally distributed across different samples, Mann-Whitney U test was applied for pairwise comparison of independent groups with mixed distributions and smaller sample sizes. Exact *p*-values and sample sizes are reported in the respective figure legends where also symbols ae explained.